Geophysical Journal International

Resistivity image beneath an area of active methane seeps in the continental slope of west Svalbard margin

Journal:	*Geophysical Journal International*
Manuscript ID	GJI-S-16-0112.R1
Manuscript Type:	Research Paper
Date Submitted by the Author:	02-Aug-2016
Complete List of Authors:	Goswami, Bedanta; University of Southampton, Ocean and Earth Science Weitemeyer, Karen; University of Southampton, Ocean and Earth Science Minshull, Tim; University of Southampton, Ocean and Earth Science; Sinha, Martin; University of Southampton, Ocean and Earth Science Westbrook, G K; University of Birmingham, School of Geography Marín-Moreno, Héctor; National Oceanography Centre Southampton. University of Southampton, Marine Geosciences
Keywords:	Gas and hydrate systems < GENERAL SUBJECTS, Arctic region < GEOGRAPHIC LOCATION, Marine electromagnetics < GEOMAGNETISM and ELECTROMAGNETISM, Non-linear electromagnetics < GEOMAGNETISM and ELECTROMAGNETISM, Electrical properties < COMPOSITION and PHYSICAL PROPERTIES, Numerical modelling < GEOPHYSICAL METHODS

GEOPHYSICAL JOURNAL INTERNATIONAL, VOL. ???, XXXX, DOI:10.1002/,

Resistivity image beneath an area of active methane seeps in the west Svalbard continental slope

Bedanta K. Goswami,[1] Karen A. Weitemeyer[1,2], Timothy A. Minshull[1],

Martin C. Sinha[1], Graham K. Westbrook[1,3,4], Héctor Marín-Moreno[2]

[1]Ocean and Earth Science, University of Southampton, National Oceanography Centre Southampton, European Way, Southampton, SO143ZH, UK

[2]National Oceanography Centre Southampton, European Way, Southampton, SO143ZH, UK

[3]School of Geography, Earth and Environmental Sciences, University of Birmingham, Birmingham, B152TT, UK

[4]Geosciences Marines, Ifremer Centre de Brest, 29280 Plouzané, France

Abstract. The Arctic continental margin contains large amounts of methane in the form of methane hydrates. The west Svalbard continental slope is an area where active methane seeps have been reported near the landward limit of the hydrate stability zone. The presence of bottom simulating reflectors (BSR) on seismic reflection data in water depths greater than 600 m suggests the presence of free gas beneath gas hydrates in the area. Resistivity obtained from marine controlled source electromagnetic (CSEM) data provides a useful complement to seismic methods for detecting shallow hydrate and gas as they are more resistive than surrounding water saturated sediments. We acquired two CSEM lines in the west Svalbard continental slope, extending from the edge of the continental shelf (250 m water depth) to water depths of around 800 m. High resistivities (5-12 Ωm) observed above the BSR support the presence of gas hydrate in water depths greater than 600 m. High resistivities (3-4 Ωm) at 390-600 m water depth also suggest possible hydrate occurrence within the gas hydrate stability zone (GHSZ) of the continental slope. In addition, high resistivities (4-8 Ωm) landward of the GHSZ are coincident with high-amplitude reflectors and low velocities reported in seismic data that indicate the likely presence of free gas. Pore space saturation estimates using a connectivity equation suggest 20-50% hydrate within the lower slope sediments and less than 12% within the upper slope sediments. A free gas zone beneath the GHSZ (10-20% gas saturation) is connected to the high free gas saturated (10-45%) area at the edge of the continental shelf,

where most of the seeps are observed. This evidence supports the presence of lateral free gas migration beneath the GHSZ towards the continental shelf.

1. Introduction

The Arctic continental margin contains large amounts of methane within hydrate bearing sediments [*Kretschmer et al.*, 2015; *Marín-Moreno et al.*, 2015b]. Methane hydrates are ice-like solid substances that are stable under high pressure and low temperature conditions [*Kvenvolden*, 1993]. Due to the cold temperatures in the Arctic, hydrate can be stable at the seafloor in around 400 m water depths for bottom water temperatures close to 2°C. Since the high latitudes are warming at a fast rate, these shallow marine hydrates are at risk of becoming unstable and dissociating [*Biastoch et al.*, 2011; *Hunter et al.*, 2013]. Methane is an important greenhouse gas, so, if large quantities of methane are released from hydrate dissociation, it may end up in the atmosphere and contribute to global warming [*Archer*, 2007].

In 2008, numerous seafloor methane seeps were reported along the 400 m isobath in the West Svalbard continental margin [*Westbrook et al.*, 2009], close to the landward edge of the gas hydrate stability zone (GHSZ). Concurrent observations of a 1°C rise in ocean temperatures over the past three decades in the area [*Westbrook et al.*, 2009] led to the suggestion of seeps originating from dissociating hydrate; a theory that is corroborated by numerical models [*Reagan and Moridis*, 2009; *Thatcher et al.*, 2013; *Marín-Moreno et al.*, 2013]. Subsequent scientific cruises to the area [*Rajan et al.*, 2012; *Berndt et al.*, 2014; *Sahling et al.*, 2014] also reported methane seeps along the 400 m isobath and discovered a number of additional seeps in shallower water depths where hydrate are not predicted to be stable. Some of these seeps were reported in water depths as shallow as 80-90 m [*Sahling et al.*, 2014]. While hydrate dissociation could be a plausible cause of the seeps around the 400 m isobath, it is unlikely to be the only factor. *Westbrook et al.* [2009] suggested up-slope migration of free gas beneath the GHSZ as another likely mechanism behind the seeps. Submersible dives have revealed colonies of methane consuming bacteria along with authigenic carbonate deposits around the 400 m isobath [*Berndt et al.*, 2014]. These deposits and recent geochemical analysis [*Panieri et al.*, 2016] suggest the presence of long term methane seepage in the area. Hydrate dissociation in response to seasonal variation in bottom water temperatures (1-2°C) was proposed as a cause for the long term seepage [*Berndt et al.*, 2014]. However, there are no pockmarks directly associated with the seep sites [*Sarkar et al.*, 2012; *Rajan et al.*, 2012; *Sahling et al.*, 2014], as one might expect in areas of prolonged focused fluid flow [*Hovland et al.*, 2002]. The absence of pockmarks may be due to the coarse glacial sediments in the area. Subsurface lithological heterogeneity between marine and glaciogenic sediments is also thought to play an important role in the location and alignment of the observed seeps [*Sarkar et al.*, 2012; *Rajan et al.*, 2012].

Gas hydrate presence beneath the continental slope of Svalbard has been inferred on the basis of bottom simulating reflectors (BSR) on seismic reflection data [*Vogt et al.*, 1994; *Westbrook et al.*, 2008; *Hustoft et al.*, 2009; *Sarkar et al.*, 2012; *Rajan et al.*, 2012] and from seismic velocity anomalies [*Westbrook et al.*, 2008; *Chabert et al.*, 2011]. This was later confirmed when gas hydrate was recovered from a shallow core at 890 m water depth [*Fisher et al.*, 2011]. Although the predicted landward edge of hydrate stability extends to around 390 m water depth, no simple BSR cutting across lithological reflectors has yet been identified in water depths shallower than 600 m [*Chabert et al.*, 2011; *Sarkar et al.*, 2012; *Ker et al.*, 2014]. A BSR is a seismic reflector that follows the seafloor but has opposite polarity. It is often caused by the phase change from solid hydrate to underlying free gas. The absence of a simple BSR could be due to increased heterogeneity where the glaciogenic sediments are more prevalent. They have a lower porosity and permeability and consequently, gas and hydrate are restricted to the more permeable marine sediment that are interbedded with the glaciogenic sediments [*Chabert et al.*, 2011]. It may also be caused by the frequency content of airgun data which results in the BSR reflection being masked by another seismic reflector [*Sarkar et al.*, 2012]. In addition, shallow free-gas signatures such as high amplitude reflectors and low-velocity anomalies are observed in the upper continental slope [*Sarkar et al.*, 2012; *Rajan et al.*, 2012] close to the methane seep sites. While seismic studies have shown evidence of shallow gas pockets around the predicted base of GHSZ [*Sarkar et al.*, 2012], they have been unable to image any gas hydrate directly linked to the seeps. Since the methane seeps must be fed either by shallow dissociating hydrate or from a free gas reservoir beneath the seafloor, improved estimates of this methane inventory are crucial. Hydrate and gas saturation estimates also provide input to models predicting the future response of the subsurface methane to ocean temperature changes [*Marín-Moreno et al.*, 2013, 2015a].

Controlled source electromagnetic (CSEM) data are sensitive to the bulk resistivity, which is affected by the presence of hydrate or/and free gas in the sediments. Hydrate and free gas are orders of magnitude more resistive than saline pore water and electrical resistivity logs are often used in drilling to detect them [*Collett and Ladd*, 2000]. The use of marine CSEM for hydrate detection was first suggested by *Edwards* [1997] and has been successful in various academic studies (e.g. *Schwalenberg et al.* [2005]; *Weitemeyer et al.* [2006a]; *Schwalenberg et al.* [2010a, b]; *Weitemeyer and Constable* [2010]; *Weitemeyer et al.* [2011];

Goswami et al. [2015]; *Attias et al.* [2016]). It was also used commercially in Japan for hydrate exploration (referenced within *Constable et al.* [2016]). In this paper, 2D resistivity cross-sections obtained from inversion of CSEM data are presented for two lines acquired in the area of methane seeps, on the west Svalbard continental slope (Figure 1). The resistivity models are then used to infer hydrate and free gas saturations for the two profiles.

2. Regional Setting

The CSEM study area (Figure 1a) is located in the continental slope of the west Svalbard margin, in the inter fan region between the Isfjorden cross-shelf trough and the Kongsfjorden cross-shelf trough, to the west of Prins Karls Forland island. The stratigraphy of the area has been influenced by early Eocene seafloor spreading and subsequent sedimentation during periods of uplift, glacio-eustatic fluctuations and sediment transport by prevailing ocean currents [*Eiken and Hinz*, 1993; *Sarkar et al.*, 2011]. The continental shelf and the upper continental slope has thick glaciogenic sediments that were deposited by Plio-Pleistocene glacial debris flows [*Solheim et al.*, 1996; *Sarkar et al.*, 2011]. The distal slope contains thick contourite sediments [*Eiken and Hinz*, 1993; *Forsberg et al.*, 1999]. On the basis of seismic velocity models, the thickness of the Cenozoic sediments in the study area varies from about 2 km near the continental shelf to about 4 km in the distal slope region [*Ritzmann et al.*, 2004].

3. CSEM Data Acquisition

The CSEM profiles were acquired using a CSEM transmitter - deep-towed active source instrument (DASI) [*Sinha et al.*, 1990], a deep-towed tri-axis electric-field receiver - Vulcan

[*Weitemeyer and Constable*, 2010; *Constable et al.*, 2016] and 14 ocean-bottom electric-field (OBE) sensors [*Minshull et al.*, 2005] (Figure 2). DASI has a 100 m long horizontal dipole antenna that was used to transmit a 1 Hz square wave current of approximately 81 A (zero to peak) during the survey. An altimeter and conductivity temperature depth (CTD) probe mounted on DASI records the tow height (∼50 m) and tow depth of the transmitter during operation. The OBEs were put on the seafloor using a small remotely operated vehicle (ROV) [*Murton et al.*, 2012] dropping them from a height of approximately 2 m. The OBEs record the horizontal components of the electric field across their two orthogonal 12 m long dipole antennae, at a sampling rate of 125 Hz. The usable range of transmitter-receiver offsets is controlled by the noise floor (10^{-13} V/Am^2) and saturation threshold (10^{-9} V/Am^2) of the pre-amplifiers used in the OBEs. Vulcan was towed at a constant offset of 350 m behind the centre of the DASI antenna using a 300 m tow rope attached to the back of the DASI antenna. The Vulcan data with a short constant offset (350 m) has high sensitivity to the shallow sediments and it complements the OBE data which are more sensitive to the deeper sediments, due to their relatively larger offsets. Vulcan records the vertical and cross-line electric fields across two orthogonal 1 m dipole antennae and the inline electric field across a 2 m dipole antenna at a 250 Hz sampling rate. A compass containing tiltmeters and pressure sensor mounted on Vulcan also records the heading, pitch, roll and depth of the instrument. Accurate positions for DASI and the ROV were obtained from an ultra-short base-line (USBL) acoustic positioning system. The position of Vulcan was estimated during data analysis by assuming it followed the DASI track.

The CSEM survey was designed with the objective of obtaining a resistivity image beneath the region where the BSR is observed within the lower slope sediments [*Sarkar et al.*, 2012] as well as the methane seeps around the 400 m isobath [*Westbrook et al.*, 2009; *Berndt et al.*, 2014; *Sahling et al.*, 2014]. Line 1 is approximately 18 km long, and was acquired in a roughly west to east direction. It starts in the lower continental slope (around 900 m water depth) and finishes at the edge of the continental shelf (around 250 m water depth). The OBE spacing was decreased gradually from 1.5 km in the west to 250 m in the east, to cover the entire area of interest with the limited number of available instruments (14 OBEs). The OBE spacing was denser to the east as most of the features of interest were in shallower water depths. Line 2 was acquired to the north of Line 1 and is 3 km long extending from around 380 m water depth to around 430 m water depth in a roughly east to west direction (Figure 1b). Only Vulcan and DASI were used to acquire this line.

4. Data Analysis

4.1. CSEM data processing

The Earth's frequency domain transfer function (TF) can be extracted from the CSEM data, which are sensitive to changes in conductivity, source-receiver offset and other geometric factors [*Constable*, 2010]. The field data, which records the voltage difference across each receiver dipole were converted to the frequency domain using a fast Fourier transform over a 1-s window length. The amplitude and phase frequency response of the pre-amplifiers within each of the receivers were used to compute a calibrated voltage, which was then divided by the receiver dipole length to calculate the electric fields. The source response was then removed by normalising the data with the source dipole moment (SDM) for each frequency to obtain the frequency domain Earth's TF. The current output by DASI was not reliably logged and only the voltage waveform was recorded for these CSEM lines. Based on analysis of other CSEM lines from the same survey that recorded the current accurately, an ideal waveform (1 Hz, 81 A) was used to compute the frequency domain SDMs. The voltage record was used to calibrate the start time of the ideal waveform to ensure phase accuracy in the frequency domain Earth's TF. Extremely noisy data outliers were manually removed and the 1-s data were then stacked to obtain a data point every 60-s, that has an improved signal to noise (S/N) ratio. This process provided data with an along-track sample interval of approximately 46 m.

Only the fundamental (1 Hz) and the first three harmonic frequencies (3, 5, 7 Hz) of OBE and Vulcan data were selected. Saturated OBE data and data below the noise floor were rejected. The OBEs saturate between 0 and 850 m offset and the maximum usable offset decreases from 2700 m at 1 Hz to 1700 m at 7 Hz. To reject air-wave contaminated data [*Constable*, 2010], the maximum usable offset was reduced for the OBE sites shallower than 350 m water depth (P09 to P13) to 2100 m at 1 Hz, decreasing to 1500 m at 7 Hz. The first 4.2 km of Line 1 were discarded due to inaccuracies in the altitude reported by the DASI altimeter (Figure 1b). This approach leaves us with no data from OBE P01 and very little data from OBE P02. In addition, data from OBEs P06 and P14 were discarded due to poorly matched electrodes. Based on S/N ratio analysis of the stacked data, all Vulcan data and most OBE data from transmissions between 1.8 and 3 km model distance on Line 1 were also rejected due to excessive noise of unknown origin.

The stacked OBE data were then rotated into the inline direction using the dipole orientations estimated by the orthogonal procrustes rotation analysis (OPRA) code [*Key and Lockwood*, 2010]. The angles obtained from OPRA were previously shown to have an accuracy of 3° [*Key and Lockwood*, 2010]. The amplitude and phase of inline OBE data were used as input into the OBE inversion. For the inversions of Vulcan data, the magnitude of the major axis of the polarization ellipse traced by the horizontal electric field vector (P_{max}) [*Smith and Ward*, 1974] was used. This approach was used because of uncertainties in Vulcan phase data, which might generate artefacts in the inversion model [*Behrens*, 2005]. The phase uncertainties arise due to ambiguities in transmitter and receiver orientations as well as unresolved timing issues between transmitter and the close offset Vulcan receiver.

4.1.1. Data Uncertainty

The standard deviation computed in each stack provides a measure of noise in the data. While the cross-line component of Vulcan contained up to 10-15% noise, the vertical component contained only about 1-2% noise and the inline component about 0.05-0.1% noise. In an ideal scenario, the recorded inline component of the electric field is along the transmitter dipole and $P_{max} = E_{inline}$. In this study, the contribution of the recorded inline component to P_{max} was greater than 98%. A 1% data error was specified for the inversion to account for navigational uncertainty.

The standard deviation of the OBE data suggest less than 1.5% noise in the inline component for the data range selected for the inversion. A composite model uncertainty analysis following *Myer et al.* [2011] suggests a maximum total uncertainty (location uncertainty, antenna dips and noise) of 2.5% for the OBE data. Based on forward model perturbations, an additional 0.5% error was assigned to account for inaccuracies in the phase of the data as a result of using an ideal waveform during processing rather than a recorded waveform. A 3% error was therefore assigned for the OBE inversion.

4.2. CSEM Inversion

The MARE2DEM code [*Key and Ovall*, 2011] was used to invert the CSEM data from the OBEs and Vulcan. OBE and the Vulcan data were inverted separately to obtain independent resistivity models. MARE2DEM uses a 2·5D finite element forward code [*Key and Ovall*, 2011] and a fast implementation of Occam's inversion [*Constable et al.*, 1987] to obtain the smoothest resistivity model from the family of models that can fit the data. It does so by automatically optimising the values of Lagrange's multiplier and model roughness [*Constable et al.*, 1987; *Key*, 2012] for the specified misfit tolerance and data error.

A simple starting model was specified containing a highly resistive air layer (10^{12} Ωm), seawater with three horizontal layers of constant resistivity (Figure 3) and a starting resistivity of 1 Ωm for the sediments beneath the seafloor. Synthetic model studies suggest a noticeable affect of seawater resistivity on the inverted resistivity of shallow sediments. However, it was not possible to specify more details for the deepest water layer because of minimum angle restrictions on triangular elements in MARE2DEM (∼30°) [*Key and Ovall*, 2011]. Specifying more detail in the bottom water layer led to minimum angle criteria being violated at the intersections of water layer boundaries and the dipping seafloor. Nevertheless, tests with a range of seawater resistivity values between 0.3 to 0.35 Ωm for the bottom layer showed that the effect of this parameter on the final OBE model was negligible. Vulcan inversions were found to be more sensitive to the seawater resistivity profile, but tests showed the chosen resistivity profile was also suitable for the Vulcan inversion. A seafloor bathymetry determined by summing the depth recorded by the CTD and altitude recorded by altimeter was specified. The air and seawater resistivity were fixed and the inversion was used to solve for the sediment resistivity. An inversion mesh of triangular elements that is finer beneath the seabed and coarser beyond the profile edges and with depth was used. The minimum edge length of the triangular elements was 50 m for the OBE inversion (26830 free parameters). Elements with smaller edge lengths led to significant extra burden on the compute times due to the large number of additional free inversion parameters. The minimum edge length was 30 m for the Vulcan inversion, in which a finer mesh for the top 600 mbsf (versus approximately 2 km for OBE inversion) was specified. Edge lengths less than 30 m are not allowed for the seafloor profile due to minimum angle restrictions ($\sim$30°). The regularised Occam inversion [*Constable et al.*, 1987] requires specification of a target misfit to produce an appropriate model. Initially, the Occam inversion was specified a low target misfit (e.g. 0 or 0.1), which is never achieved. An appropriate target misfit was then estimated by analysing the variation of misfit with Lagrange's multiplier in this initial inversion. The lowest root mean square (RMS) misfit achieved in the initial inversion was chosen as the target misfit and the inversion was re-run with the new target value (Table 1).

Two-dimensional resistivity models inverted from inline CSEM data are sensitive to horizontal as well as vertical resistivity [*Constable*, 2010; *Ramananjaona et al.*, 2011; *MacGregor and Tomlinson*, 2014]. Both isotropic and vertical transverse isotropic (VTI) ($\rho_x = \rho_y \neq \rho_z$) inversions were therefore run for the CSEM lines with a horizontal to vertical smoothing ratio of 3:1. Anisotropic penalty was 1 for the VTI inversions. The two inversions resulted in very similar resistivity models for the chosen target misfits. However, the horizontal resistivity models obtained from the VTI inversion are unlikely to be suitable for detailed analysis as no cross-line data were used [*Ramananjaona et al.*, 2011]. Nevertheless, in the presence of anisotropy, the smooth vertical resistivity models obtained from VTI inversions are expected to be more accurate than those obtained from an isotropic inversion [*Ramananjaona et al.*, 2011; *MacGregor and Tomlinson*, 2014; *Myer et al.*, 2015], and in the absence of anisotropy, identical to the results of an isotropic inversion [*Myer et al.*, 2015]. Therefore, the focus of the discussions is on the smooth vertical resistivity models from the VTI inversions. The isotropic inversion models are also shown in the supplementary figures (Figures S1 and S2) to demonstrate similarity to the vertical resistivity models.

5. Resistivity models

5.1. Line 1 Vulcan Inversion

The vertical resistivity model obtained from VTI inversion of Vulcan data shows significant lateral resistivity variation in the shallow subsurface (Figure 4a). A good fit between data and model (Figure 4b) is observed for Line 1. Synthetic data generated for a dipping antenna were inverted using the known as well as no dip information. Observation of residuals of these synthetic tests suggest lack of DASI antenna dip information is a likely cause of the small frequency dependent bias on the normalised residuals (Figure 4c). A zone of 4-12 Ωm resistivity is observed within the lower slope sediments (700-800 m water depth) between 0 and 2 km model distance. Similar high resistivity is also observed on the resistivity model of a crossing-line at the western edge of Line 1 (Figure S3). A resistivity of 3-4 Ωm is then observed from 4 to 10.5 km model distance within the upper slope sediments (approximately 675-380 m water depth) (Figure 4a). The resistivity increases eastwards reaching 5-8 Ωm, with pockets of around 10 Ωm, within the upper continental slope sediments between 11 and 14 km model distance (water depths of around

210-380 m). The resistivity decreases with depth to the starting model resistivity of 1 Ωm, throughout the profile.

5.2. Line 1 OBE Inversion

The vertical resistivity model obtained from VTI inversion of the OBE data (Figure 5) shows 3–4 Ωm resistivity within the top 200 mbsf between 0 and 8 km model distance. A good fit between data and model (Figure 6) is also observed for the OBE inversions. A thin resistive feature with 4–6 Ωm resistivity is observed approximately 100 mbsf at 8 km model distance which becomes gradually shallower landward, eventually reaching the seafloor around 12.5 km model distance. Resistivities of 1.5–2 Ωm are observed between 200 mbsf and 1000 mbsf with few regions containing values of 3–4 Ωm. Beneath 1000 mbsf, the resistivity gradually increases to around 12–15 Ωm.

5.3. Line 2

The vertical resistivity model (Figure 7a) obtained from VTI inversion of Vulcan P_{max} data for Line 2 shows a steady increase in resistivity from west to east within the shallow subsurface sediments. The resistivity of 3–4 Ωm beneath water depths of 410 m (1.5 km model distance) to 430 m (3 km model distance) gradually increases to 5–8 Ωm resistivity for water depths shallower than 410 m (0–1.5 km model distance). A good fit between data and model predictions (Figure 7b) is observed for Line 2.

6. Discussion

Two sets of EM receivers (Vulcan and OBEs) were used in this survey with an aim to resolve both shallow and deep subsurface resistivity features. Although the Occam inversion outputs the smoothest model, it is also possible to fit more complicated models to the data for the given error. Unlike a Bayesian inversion [*Chen et al.*, 2007; *Ray and Key*, 2012; *Buland and Kolbjørnsen*, 2012], it does not provide any information about model uncertainty. Finding the suite of these models would require the application of many perturbations to the final model, that is impractical, given model run times (On 64 computer nodes 4x Xeon E5/Core i7 processors, the OBE inversions take approximately 20 hours and the Vulcan inversions take approximately 14 hours for Line 1 and 8 hours for Line 2). Another important consideration while interpreting the models is to determine whether any of the features seen are inversion artefacts. The resistivity models obtained from the inline CSEM data are primarily sensitive to transverse resistance [*Constable*, 2010] (the product of resistivity and thickness). When we consider the nature of the inversion approach, the variation in the size of the inversion grids with depth, and the trade-off between resistivity and thickness to recover the transverse resistance, it is difficult to quantify the resolution of the models. It would also require careful consideration of the dependence on frequency, available data range, noise and data errors in any such analysis [*Constable*, 2010]. Synthetic model inversions can provide qualitative but useful information about sensitivity and resolution [*Myer et al.*, 2015; *Goswami et al.*, 2015], and we take this approach here. The synthetic models generated using the frequencies of interest (1, 3, 5 & 7 Hz) are used to estimate the maximum depth sensitivity of Vulcan and sensitivity of the CSEM experiment to shallow and deep features observed in the resistivity models.

6.1. Vulcan depth sensitivity

The Vulcan P_{max} data is computed for a single, short (350 m) source-receiver offset. Therefore, the data overlap for the Vulcan inversion is proportional to the number of frequencies used. The Vulcan inversion models are only expected to be sensitive to the very shallow sediments (150–250 m). The sensitivity matrix obtained from the Jacobian of the Occam inversion [*Constable et al.*, 1987] provides information about the data's sensitivity to model parameters. These suggest 50% sensitivity to model paramters around 400 mbsf (e.g. Figures 4a & 7a). We used 2D synthetic models and inversions to further understand the depth sensitivity of the Vulcan P_{max} data. For the synthetic tests, DASI and Vulcan are assumed to maintain a constant altitude of 50 m above a flat seafloor at 750 m water depth, with a separation of 350 m. The Earth is assumed to be isotropic, consisting of an insulating air layer (10^{12} Ωm), conducting seawater of 0.3 Ωm and resistive sediments. In the first scenario, a 3 Ωm overburden of varying thickness is assumed to terminate at a 0.3 Ωm conductive half-space (Figure 8a). A 0.3 Ωm resistivity is chosen for the terminating conductor to help with interpretation as it is significantly lower than starting model resistivity of 1 Ωm. Vulcan inversion models result in a terminating conductor that fall back to the starting half-space of 1 Ωm (e.g. Figure 7). For the second scenario, a 1 Ωm overburden resistor of varying thickness and a 5 Ωm terminating resistor was assumed (Figure 8b). The thickness of the overburden layer is varied from 100 m to 350 m (Figure 8a & b). Random Gaussian noise was added to the synthetic data that is similar to the noise in the real data (0.1% of datum) for both model scenarios. A starting model consisting of fixed air and water layers from the true model and starting sediment resistivity of 1 Ωm was specified. The minimum edge length of the triangular mesh is set to be 30 m for the top 1000 mbsf, increasing in size with depth and towards the ends of the synthetic profile. The inversions of both synthetic models converged to the target misfit of 1 within 10 iterations producing a good model fit to data.

Since inline CSEM data is mainly sensitive to the transverse resistance (resistivity x layer thickness) for the chosen water depths [*Constable*, 2010; *MacGregor and Tomlinson*, 2014] and the Occam inversion outputs a smooth model, a combination of transverse resistance and resistivity is the preferred way to qualify sensitivity to a subsurface feature. Based on observations of various synthetic tests, the inverted transverse resistance of the overburden layer recovered to within 15% of true value is considered a criterion for sensitivity. The inverted resistivity of the terminating layer recovered to within ~33% of true resistivity is considered as another criterion for sensitivity. The resistivity tolerance is much higher than the transverse resistance threshold because it is easier to identify 0.1 Ωm resistivity differences in the inversion results, which is ~33% for the 0.3 Ωm terminating conductor. For both the terminating conductor (Figure 8a, Table 2) and terminating resistor (Figure 8b, Table 3) tests, the joint transverse resistance and resistivity tolerances are satisfied by the models up to 250 m overburden thickness. There is an arguable sensitivity for the 300 m model, but we suggest a conservative estimate of 250 m for Vulcan depth sensitivity based on this analysis. The synthetic tests along with the Jacobian sensitivity overlays suggest the high resistivity zones in the Vulcan inversion models (Figure 4a & Figure 7a) are therefore likely to be real features.

6.2. Shallow resistivity

Shallow resistive features can be observed in all of the resistivity models. The Vulcan depth sensitivity tests (Figure 8) suggest that the shallow resistive zones observed in the Vulcan models are real. The Vulcan models (Figure 4) are expected to better resolve the shallow resistivity between 0 and 8 km model distance than the OBE models (Figure 5) due to the relatively large minimum usable offset (850 m) and large spacing between OBEs. However, the models differ more between 0 and 2 km model distance (Figure 4 and Figure 5) than elsewhere. This difference arises because only long range (large transmitter-receiver offset) OBE data are available between 0–3 km model distance due to issues with transmitter altitude and noise (discussed in Section 4.1). This issue causes poor resolution of the shallow resistivity in the OBE models in this area.

Synthetic models with an ideal survey geometry are used to compare sensitivity to shallow resistors in OBE and Vulcan inversions. An insulating air layer (10^{12} Ωm), 0.3 Ωm seawater resistivity, a flat seafloor at 750 m water depth with sediment half-space resistivity of 3 Ωm is assumed. A 2.2 km long and 100 m thick resistor is designed to be buried 50 mbsf, between 1 and 3.2 km model distance (Figure 9a). The synthetic Vulcan P_{max} data are generated for DASI and Vulcan at 50 m above the seafloor. Synthetic amplitude and phase OBE data are generated for OBEs placed at 1, 2.5, 4 and 7 km model distance to simulate the large spacing between OBEs in the deep waters. Random noise with a Gaussian distribution that is 0.1% and 2% of datum was added to Vulcan and OBE synthetic data respectively. The same starting model and inversion mesh is used as the Vulcan sensitivity tests. Both OBE and Vulcan synthetic model inversions converged in five iterations to the target misfit of 1 with a good model fit to data. The synthetic inversions show that the Vulcan model (Figure 9b) is better at recovering the shape and lateral extent of the shallow resistor compared to the OBE model (Figure 9c). Vulcan also appeared to be able to provide a better limit on the depth of the lower boundary of the resistor. However, both inversions recovered similar resistivity (6–8 Ωm instead of 10 Ωm true resistivity) for the shallow resistor. The inversions of both the OBE and Vulcan data are therefore expected to be sensitive to shallow resistive features. The inversion of the Vulcan data provide a more accurate representation of the shallow features due to the short offset data collected with Vulcan and the saturation limits of the OBE data (0–850 m offsets).

6.3. Gas hydrate and free gas

The models show both vertical and lateral variation in sub-surface resistivity. The bulk resistivity of sediments depends on various factors such as porosity, pore fluid saturation, pore fluid salinity, temperature, mineralogy and grain fabric of the host sediments [*Ellis et al.*, 2010] which are poorly known for the study area. Coincident seismic reflection datasets JR211-03 (for Line 1) and JR211-09 (for Line 2) [*Sarkar et al.*, 2012], however, provide some constraints to help with the interpretation of the shallow (0-400 mbsf) sub-surface sediments.

6.3.1. Interpretation of resistivity models

The thickness of the predicted GHSZ obtained from the non-steady state hydrate stability models of *Marín-Moreno et al.* [2013] varies from approximately 200 m at 800 m water depth to 0 m at around 390 m water depth. The models from the Vulcan inversions are therefore used for the interpretation of the GHSZ, as they are likely to be more sensitive to the top 250 mbsf. A BSR on JR211-03 [*Sarkar et al.*, 2012] beneath the 4–12 Ωm resistivity between 0 and 2 km model distance on Line 1 suggests that the high resistivity zone may be caused by the presence of hydrate in water depths greater than 700 m (Figure 10). The region of 3–4 Ωm resistivity within the GHSZ, between 4 and 10.5 km model distance on Line 1 (Figure 10) and 1–3 km model distance on Line 2 (Figure 11) does not contain any seismic signatures that indicate hydrate on the seismic reflection data.

However, *Chabert et al.* [2011] suggest some hydrate in these water depths on the basis of high velocity anomalies. The resistivity of these shallow sediments are higher than the resistivity of hemipelagic sediments recorded at ODP Site 986 [*Jansen et al.*, 1996] (Figure 12a), where no direct evidence of hydrate presence was documented. Although ODP Site 986 is located in 2036 m water depth and approximately 300 km to the south west of the study area (Figure 1), it is the only available nearby resistivity log. If we assume that there are no significant differences in porosity and sediment composition between the study area and ODP Site 986, the higher resistivity may indicate the presence of hydrate in the shallow sediments between 4 and 10.5 km. High resistivities landward of the predicted GHSZ are also observed on both Line 1 (Figure 10) and Line 2 (Figure 11) which is consistent with the low velocity zones and bright amplitude reflectors seen in seismic data and may indicate the presence of shallow free gas accumulations [*Sarkar et al.*, 2012]. However, higher resistivities in the upper slope sediments may also result from reduction in porosity due to increased heterogeneity and glacial content in the area [*Chabert et al.*, 2011; *Sarkar et al.*, 2012].

Direct comparison of our resistivity models with other hydrate bearing areas of the world is difficult due to limited number of such studies and difference in the parameters affecting resistivity across the various hydrate provinces. If the porosity and background resistivity of the ODP Site 986 [*Jansen et al.*, 1996] is assumed to be valid for the study area, the resistivities for the GHSZ can be compared to areas with similar porosity (50-60%) and background resistivity (1–1.5 Ωm). The comparison can be limited further to resistivities in areas of hydrate presence derived from CSEM studies only for a like-to-like comparison. Resistivities of 3–12 Ωm in the Hikurangi Margin, offshore New Zealand [*Schwalenberg* *et al.*, 2010a], around 4 Ωm in Porangahau Ridge, offshore New Zealand [*Schwalenberg et al.*, 2010b], 3–5 Ωm in the Cascadia margin [*Schwalenberg et al.*, 2005], and no greater than 5 Ωm for the Hydrate Ridge [*Weitemeyer et al.*, 2006b, 2011] were reported, which are comparable to the values of resistivity reported here. These sites, however, were all in deeper water, with a more distal sediment supply without any glaciogenic component.

6.3.2. Estimating hydrate and free gas saturations

The resistivity models were used to infer pore space hydrate and free gas saturations in the study area. Considering the lack of direct information about many of the parameters affecting bulk resistivity in the area, quantitative interpretation of the resistivity models will contain large uncertainties. However, sensible values of porosity, pore fluid salinity and temperature may be obtained from previous geological, geophysical and oceanographic studies in the west Svalbard margin. Due to the similar influence of ocean currents on the depositional history of the continental basin and slope sediments [*Eiken and Hinz*, 1993], ODP Site 986 is assumed to be fairly representative of the lithology of the slope sediments. Similarity in the porosity derived from seismic velocity at the Site S2 (water depth of 500 m) [*Chabert et al.*, 2011], at the northern boundary of the study area and porosities observed at ODP Site 986 suggests the assumption of ODP Site 986 porosity is reasonable for the mid to deep slope. An exponential least-squared fit to the ODP porosity log (Figure 12) was therefore used for the saturation estimates.

Since the presence of glacial sediments at the upper slope is likely to cause reduction in porosity [*Chabert et al.*, 2011; *Sarkar et al.*, 2012], gas and hydrate saturations for this area were also estimated using an average porosity of 35%, similar to that used by *Marín-Moreno et al.* [2013] and *Marín-Moreno et al.* [2015a]. Bottom water temperature variations in the area are available from the DASI CTD for 50 m above the seafloor. Pore-water resistivities were estimated using the bottom water temperatures and an average geothermal gradient of 55°C/km [*Sarkar et al.*, 2012] using the relationship of *Becker* [1985]. The commonly used Archie's equation [*Archie*, 1942], was used to obtain hydrate and free gas saturations and can be expressed as:

$$S_w = \left[\frac{\rho_w a \phi^{-m}}{\rho}\right]^{\frac{1}{n}} \tag{1}$$

for pores partially filled with water and hydrate and/or gas. Here, S_w is the pore water saturation, ρ_w is the pore-water resistivity, ρ is the estimated resistivity, ϕ is the porosity and n is the saturation coefficient. The tortuosity constant, a, and cementation constant, m, are both related to the interconnection of pores in the sediment matrix. The degree of pore saturation of resistive material (hydrate and/or gas), S_R is then calculated from water saturation using:

$$S_R = 1 - S_w \tag{2}$$

Commonly used values of a=1 and m=n=2 were found to fit the background resistivity trend derived from ODP Site 986. However, clay is abundant in the study area [*Eiken and Hinz*, 1993; *Forsberg et al.*, 1999], which requires a different equation to account for the additional clay conductivity effects [*Mavko et al.*, 2009]. Due to lack of well logs to obtain required parameters, it was not feasible to use *Waxman and Smits* [1968]'s equation to account for clay conductivity effect. A modified connectivity equation [*Montaron*, 2009; *Lee*, 2011], which provides an empirical approach to account for clay conductivity was used, to provide an alternative estimate of the hydrate and free gas saturations. The connectivity equation can be expressed as:

$$\rho = \frac{a\rho_w}{(\phi S_w - \chi_w)^{\mu}} \tag{3}$$

which can be rearranged to

$$S_w = \frac{1}{\phi}\left[(\frac{a\rho_w}{\rho})^{\frac{1}{\mu}} + \chi_w\right] \tag{4}$$

Here, χ_w is the water connectivity index [*Montaron*, 2009]. χ_w is expected to lie between -0.2$\leq\chi_w\leq$+0.2 and can be approximated using the equation given by *Lee* [2011]:

$$\chi_w = \alpha C_v \phi^{\mu} S_w \tag{5}$$

where C_v is the clay percentage, μ is the conductivity coefficient, which ranges between 1.6 and 2, and α is an adjustable parameter determined from data with known ϕ and S_w [*Lee*, 2011]. In absence of direct constraints, μ=m=2, water saturated sediments (S_w=1) and C_v values obtained from *Forsberg et al.* [1999] were used to calculate sediment resistivity using equations 3 and 5 for different values α. A value of α=3 provided a good fit for the calculated sediment resistivity to the observed ODP Site 986 resistivity [*Jansen et al.*, 1996] (Figure 12b). The calibrated value of α was then used to obtain the alternative hydrate and free gas saturation within the shallow sediments using equations 2, 4 and 5. Both Archie's equation and the connectivity equation assumed that hydrate and free gas replace pore waters and therefore provide saturation estimates as percentage of pore space which are shown in Table 4. In absence of velocity constraints, only hydrate presence is assumed as the cause of high resistivity within the predicted GHSZ. Free gas is assumed to be the cause of high resistivities outside the predicted GHSZ. However, hydrates can occupy veins and fractures in fine grained marine sediments [*Lee and Collett*, 2009; *Cook et al.*, 2010], which is not accounted for by the two methods. Nevertheless, the inferred

488 hydrate saturations (Table 4) lie between the extremal bounds of saturation obtained us-
489 ing Hashin-Shtrikman (H–S) bounds of effective conductivity [*Schmeling*, 1986] assuming
490 100 Ω for the resistivity of rock matrix. The H–S upper bound, which assumes conductive
491 spherical inclusions within a resistive matrix, may better represent hydrates in fractures
492 and veins [*Weitemeyer et al.*, 2011]. Use of this bound suggests 70–90% hydrate satura-
493 tion within the pore spaces of the GHSZ (35–48% of bulk volume), whereas no hydrate
494 saturation is obtained using the H–S lower bounds as the resistivities observed in our
495 model are too low for this estimate.

496 Depth averaged free gas saturations were also inferred for incremental 100 m thick layers
497 beneath the predicted base of GHSZ, using the OBE resistivity model for Line 1 (Fig-
498 ure 13). A gradual increase in free gas saturation from 2-20% at the lower slope sediments
499 (0–2 km model distance, Figure 13a) to 15–55% at the edge of continental shelf (8–13 km
500 model distance, Figure 13a) was inferred for the first layer directly beneath the GHSZ.
501 However, the maximum free gas saturation reduces to around 38% when a lower porosity
502 of 35% was used for these estimates for the upper slope sediments (Figure 13a). The aver-
503 age free gas saturations for the upper slope sediments was inferred to gradually decrease
504 to the same level as the lower slope sediments in the subsequent layers (Figure 13).

505 **6.3.3. Interpretation of hydrate saturation estimates**

506 The hydrate saturations inferred here are within the range of estimates suggested in
507 other hydrate provinces such as the Cascadia margin [*Schwalenberg et al.*, 2005] (up to
508 50%), Hydrate Ridge [*Weitemeyer et al.*, 2011] (up to 49%) Porangahau Ridge [*Schwalen-*
509 *berg et al.*, 2010a] (up to 17%) and Hikurangi margin (26–68%), where resistivity from
510 CSEM data were used for pore space saturation estimates using Archie's equation. The

inferred hydrate saturations for the lower slope sediments, between 0–2 km model distance on Line 1 (Table 4) are, however, higher than previous estimates in the deepwater area based on seismic velocities [*Westbrook et al.*, 2008; *Hustoft et al.*, 2009; *Chabert et al.*, 2011]. These studies suggest a maximum hydrate saturation of 22% [*Chabert et al.*, 2011] and 2–25%[*Westbrook et al.*, 2008] at around 1300 m water depth. A 20% reduction in the porosity of the top 100 mbsf ($\sim$ 45% to 25%) is required to better match the published deep water hydrate saturation estimates ($\sim$20%), using the resistivities between 0–2 km on Line 1 and the connectivity equation (Equation 3). The inferred hydrate saturations for the mid and upper slope sediments (2–10.5 km model distance on Line 1; 1–3 km model distance on Line 2, Table 4) are also considerably higher than 2–5% hydrate saturation for OBS sites N2 (866 m water depth) and S2 (480 m water depth) [*Chabert et al.*, 2011] assuming the ODP Site 986 derived porosity trend. They are however comparable to the hydrate saturations estimated using 35% average porosity between 8–10.5 km model distance on Line 1 and 1–3 km model distance on Line 2 (Table 4).

Modeling studies suggest that the GHSZ beneath 400–430 m water depth in the study area is vulnerable to increase in bottom water temperatures within the next century [*Marín-Moreno et al.*, 2013, 2015a]. Extrapolating the inferred average hydrate saturation for the seafloor depths of 400–430 m (15–45% between 9–10.5 km model distance on Line 1, Table 4) to the 11 km long zone of active methane seeps in Area 3 reported by *Sahling et al.* [2014], 2530-7600 Gg of carbon (C) is inferred within this vulnerable hydrate reservoir. However, on assuming the reduced porosity of 35% for the GHSZ within the upper slope and a maximum of 12% hydrate saturation (Table 4), around 1310 Gg of carbon is inferred within this vulnerable zone. These estimates are presented assuming that the seafloor profile for Line 1 and Line 2 are representative for the entire Area 3 between 400–430 m water depth. The amount of carbon available for dissociation from hydrates in our estimates is an order of magnitude higher than the amount *Marín-Moreno et al.* [2015a] predicts may release in the next 100 years. The model estimates of *Marín-Moreno et al.* [2015a] suggest only a part of the hydrate in the vulnerable zone will dissociate and some of the methane from dissociation will stay in the seabed as free gas.

6.3.4. Interpretation of free gas saturation estimates

The inferred free gas saturations at the landward edge of hydrate stability using both Archie and connectivity methods are very high. Such high saturations may overpressure the sediments located within the free gas zone and facilitate the flow of free gas towards the surface [*Hornbach et al.*, 2004]. A ∼20% further reduction in the ODP derived porosity (∼45% to 25%) near the continental shelf edge would be required to obtain an average free gas saturation of 3–10% as suggested by *Chabert et al.* [2011]. Actual free gas saturations at the continental shelf edge are therefore likely to be lower than our estimates. However, high free gas saturations are likely to be present since the seeps on the upper slope and the continental shelf are still active [*Westbrook et al.*, 2009; *Berndt et al.*, 2014; *Sahling et al.*, 2014] and are controlled by sub-surface lithological variations [*Sarkar et al.*, 2012]. The vertical resistivity model from OBE inversion for Line 1 (Figure 5) also shows high resistivities beneath the GHSZ, that are likely caused by the presence of free gas (Figure 13). Previous estimates in the west Svalbard margin suggest 2–7% of pore spaces saturated by free gas directly beneath the GHSZ and up to 9% free gas saturation in lower slope sediments [*Chabert et al.*, 2011]. Average free gas saturations of around 8–50% are inferred using Archie's equation and 2–48% using the connectivity equation, beneath the GHSZ.

The free gas zone beneath the GHSZ is also linked to the free gas zone at the edge of the continental shelf suggesting possible up-slope migration of free gas beneath the GHSZ *Westbrook et al.* [2009]. A rough estimate using the inferred free gas saturations outside the GHSZ (Figure 13) shows a large amount of carbon present in the form of free gas (Figure 14). There is potentially more carbon in free gas form than within hydrates in the Area 3 [*Sahling et al.*, 2014].

On the basis of seismic velocity structure [*Ritzmann et al.*, 2004], the depth to the basement in our study area is estimated to be around 2–3 km beneath the seafloor at the eastern part of our profile with the sediment thickness increasing from east to west [*Ritzmann et al.*, 2004]. The deep resistivity feature in our model (6–17 Ωm) is therefore unlikely to be the basement as it is shallower than 2 km. In addition, basement rocks are likely to have resistivity greater than 100 Ωm. Synthetic model studies using the real survey parameters indicate that the resistive feature at the depth of the observed deep resistivity can be resolved by the data only in presence of a thick (>10 km) high resistivity (100 Ωm) beneath (Figure S4). The deep resistive feature in our OBE model may therefore be caused by low porosity lithified sediments overlying the basement.

7. Conclusion

We analysed seafloor and towed receiver CSEM data along with high resolution seismic reflection data in a region of active methane seeps at the continental slope of west Svalbard margin. It has provided additional evidence and constraints for hydrate and free gas presence along the continental slope and at the continental shelf edge (Figure 15). This study also provided a first look at the subsurface resistivity structure of the continental slope area. The new resistivity information should help future studies to design more targeted electromagnetic studies in the area. Based on our analysis, we conclude that:

1. High resistivities (4–12 Ωm) within the predicted GHSZ and the presence of BSR in coincident seismic reflection data, suggest the presence of gas hydrate in the lower slope sediments. Average gas hydrate saturations of around 15–55% are inferred here.

2. High resistivities (3–4 Ωm) within the predicted GHSZ of the upper slope sediments provide geophysical evidence for hydrate presence in the area. Up to 12% average hydrate saturation is inferred for the upper slope sediments.

3. High resistivities around the landward edge of the GHSZ are consistent with low velocities and the presence of high amplitude reflectors in coincident seismic data [*Sarkar et al.*, 2012] suggesting high free gas saturations. A free gas zone beneath the GHSZ with more than 10% gas saturation is inferred to be linked to the zone of free gas escaping from the seabed near the continental shelf.

4. There is thus a large volume of carbon in the form of free gas within the upper slope sediments.

Acknowledgments. We are grateful to the Captain, crew and shipboard scientific party of the RRS James Clark Ross cruise JCR269B for their hard work at sea. We are also thankful to Veit Huehnerbach for operating HyBIS, Laurence North and Yee Yuan Tan for their time during DASI operation and former PhD students, Amelia Astley, Anupama Rajan, Carolyn Graves, Helen Miller and Joan Campanya i Llovet for their hard work during the cruise. We would also like to thank Natural Environment Research Council's Ocean Bottom Instrumentation Facility and especially Ben Pitcairn and Robert

Kirk for their onboard technical support. This research would not have been possible without the funding of the National Environment Research Council (NERC), UK (grant NE/H002732/1 and NE/H022260/1). Minshull is supported by a Wolfson Research Merit award. Seismic and CSEM data are archived at the British Oceanographic Data Centre. We thank Kerry Key for developing the MARE2DEM code and making it publicly available and David Myer for the CSEM processing codes and valuable discussions. We thank reviewers Katrin Schwalenberg and Ann Cook for their suggestions to improve the manuscript.

References

Archer, D. (2007), Methane hydrate stability and anthropogenic climate change, *Biogeosciences*, *4* (4), 521–544, doi:10.5194/bg-4-521-2007.

Archie, G. E. (1942), The electrical resistivity log as an aid in determining some reservoir characteristics, *Transactions of the American Institute of Mining Engineers*, *146*, 54–62.

Attias, E., K. A. Weitemeyer, T. A. Minshull, A. Best, M. C. Sinha, M. Jegen-Kulcsar, S. Holz and C. Berndt (2016), Controlled-source electromagnetic and seismic delineation of sub-seafloor fluid flow structures in a gas hydrate province, offshore Norway, *Geophysical Journal Int.*, doi:10.1093/gji/ggw188.

Becker, K. (1985), Large scale electrical resistivity and bulk porosity of the oceanic crust, deep sea drilling project hole 504B, *Tech. rep.*, Initial Report, Deap Sea Drilling Project.

Becker, K. (1990), Large-scale electrical resistvity and bulk porosity of the upper oceanic crust at Hole 395A, in *Proceedings of the Ocean Drilling Program, Scientific Results*, vol. 106, pp. 205–212.

621 Behrens, J. P. (2005), The Detection of Electrical Anisotropy in 35 Ma Pacific Lithosphere: Results from a Marine Controlled-Source Electromagnetic Survey and Implications for Hydration of the Upper Mantle, Ph.D. thesis, University of California, San Diego.

624 Berndt, C., et al. (2014), Temporal Constraints on Hydrate-Controlled Methane Seepage off Svalbard., *Science (New York, N.Y.)*, *284*, doi:10.1126/science.1246298.

626 Biastoch, A., et al. (2011), Rising Arctic Ocean temperatures cause gas hydrate destabilization and ocean acidification, *Geophysical Research Letters*, *38*(8), doi:10.1029/2011GL047222.

629 Buland, A., and O. Kolbjørnsen (2012), Bayesian inversion of CSEM and magnetotelluric data, *Geophysics*, *77*(1), E33–E42, doi:10.1190/geo2010-0298.1.

631 Chabert, A., T. A. Minshull, G. K. Westbrook, C. Berndt, K. E. Thatcher, and S. Sarkar (2011), Characterization of a stratigraphically constrained gas hydrate system along the western continental margin of Svalbard from ocean bottom seismometer data, *Journal of Geophysical Research*, *116*(B12), B12,102, doi:10.1029/2011JB008211.

635 Chen, J., G. M. Hoversten, D. Vasco, Y. Rubin, and Z. Hou (2007), Special Section — Marine Controlled-Source Electromagnetic Methods: A Bayesian model for gas saturation estimation using marine seismic AVA and CSEM data, *Geophysics*, *72*(2), WA85–WA95.

638 Collett, T. S., and J. Ladd (2000), Detection of Gas Hydrate with Downhole Logs and Assessment of Gas Hydrate Concentrations (Saturations) and Gas Volumes on the Blake Ridge with Electrical Resistivity Data, in *Proceedings of the Ocean Drilling Program, Scientific Results*, vol. 164, pp. 179–191.

642 Constable, S. C., Kannberg, P. K, and Weitemeyer, K. A (2016), Vulcan: A deep-towed CSEM receiver, *Geochem. Geophys. Geosyst.*, *17*, 1042–1064, doi:

10.1002/2015GC006174

Constable, S. (2010), Ten years of marine CSEM for hydrocarbon exploration, *Geophysics*, *75*(5), 75A67–75A81.

Constable, S. C., R. L. Parker, and G. Constable (1987), Occam's Inversion: A practical algorithm for generating smooth models from electromagnetic sounding data, *Geophysics*, *52*(3), 289–300.

Cook, A.E., Anderson, B. I., Malinverno, A., Mrozewski, S., and Goldberg, D.S. (2010), Electrical anisotropy due to gas hydrate-filled fracture planes, *Geophysics* *75*(6), F173–F185, doi:10.1190/1.3506530

Edwards, R. N. (1997), On the resource evaluation of marine gas hydrate deposits using sea-floor transient electric dipole-dipole methods, *Geophysics*, *62*(1), 63–74.

Eiken, O., and K. Hinz (1993), Contourites in the Fram Strait, *Sedimentary Geology*, *82*(1-4), 15–32, doi:10.1016/0037-0738(93)90110-Q.

Ellis, M. H., M. C. Sinha, T. A. Minshull, J. Sothcott, and A. I. Best (2010), An anisotropic model for the electrical resistivity of two-phase geologic materials, *Geophysics*, *75*(6), E161–E170, doi:10.1190/1.3483875.

Fisher, R. E., et al. (2011), Arctic methane sources : Isotopic evidence for atmospheric inputs, *Geophysical Research Letters*, *38*, 3–8, doi:10.1029/2011GL049319.

Forsberg, C. F., A. Solheim, E. Jansen, and E. S. Andersen (1999), The Depositional Environment of the Western Svalbard Margin During the Late Pliocene and the Pleistocene: Sedimentary facies at Site 986, in *Proceedings of the Ocean Drilling Program, Scientific Results*, vol. 162, pp. 233–246.

Goswami, B. K., Weitemeyer, K. A., Minshull, T. A., Sinha, M. C., Westbrook, G. K., Chabert, A., Henstock, T. J., and Ker, S. (2015), A joint electromagnetic and seismic study of an active pockmark within the hydrate stability field at the Vestnesa Ridge , West Svalbard margin, *Journal of Geophysical Research*, *120*(10), 6797–6822.

Hornbach, M. J., D. M. Saffer, and W. S. Holbrook (2004), Critically pressured free-gas reservoirs below gas-hydrate provinces, *Nature*, *427*(January), 142–144.

Hovland, M., J. V. Gardner, and A. G. Judd (2002), The significance of pockmarks to understanding fluid flow processes and geohazards, *Geofluids*, *2*, 127–136.

Hunter, S., D. Goldobin, A.M. Haywood, A. Ridgwell, and J. Rees (2013), Sensitivity of the global submarine hydrate inventory to scenarios of future climate change, *Earth and Planetary Science Letters*, *367*, 105–115, doi:10.1016/j.epsl.2013.02.017.

Hustoft, S., S. Bünz, J. Mienert, and S. Chand (2009), Gas hydrate reservoir and active methane-venting province in sediments on <20 Ma young oceanic crust in the Fram Strait, offshore NW-Svalbard, *Earth and Planetary Science Letters*, *284*(1-2), 12–24, doi:10.1016/j.epsl.2009.03.038.

Jakobsson, M., R. Macnab, L. Mayer, R. Anderson, M. Edwards, J. Hatzky, H. W. Schenke, and P. Johnson (2008), An improved bathymetric portrayal of the Arctic Ocean: Implications for ocean modeling and geological, geophysical and oceanographic analyses, *Geophysical Research Letters*, *35*(7), doi:10.1029/2008GL033520.

Jansen, E., M. Raymo, and P. Blum (1996), Shipboard Scientific Party 2 Hole 986A, in *Proceedings of the Ocean Drilling Program, Initial Reports*, vol. 162, pp. 287–342.

Ker, S., Y. Le Gonidec, B. Marsset, G. K. Westbrook, D. Gibert, and T. a. Minshull (2014), Fine-scale gas distribution in marine sediments assessed from deep-towed seismic data, *Geophysical Journal International*, *196*(3), 1466–1470, doi:10.1093/gji/ggt497.

Key, K. (2012), Marine EM inversion using unstructured grids: A 2D parallel adaptive finite element algorithm, in *SEG Las Vegas 2012 Annual Meeting*, 9, pp. 1–5, doi: http://dx.doi.org/10.1190/segam2012-1294.1.

Key, K., and A. Lockwood (2010), Determining the orientation of marine CSEM receivers using orthogonal Procrustes rotation analysis, *Geophysics*, *75*(3), F63–F70, doi: 10.1190/1.3378765.

Key, K., and J. Ovall (2011), A parallel goal-oriented adaptive finite element method for 2.5D electromagnetic modelling, *Geophysical Journal International*, *186*(1), 137–154, doi:10.1111/j.1365-246X.2011.05025.x.

Kretschmer, K., A. Biastoch, L. Rüpke, and E. Burwicz (2015), Modeling the fate of methane hydrates under global warming, *Global Biogeochem. Cycles*, *29*, 610–625, doi: 10.1002/2014GB005011..

Kvenvolden, K. (1993), Gas Hydrates- geological perspective and global change, *Reviews of Geophysics*, *31*(2), 173–187.

Lee, M. W., and Collett, T. S. (2009), Gas hydrate saturations estimated from fractured reservoir at Site NGHP-01-10, Krishna-Godavari Basin, India, *Journal of Geophysical Research*, doi:10.1029/2008JB006237

Lee, M. W. (2011), Connectivity Equation and Shaly-Sand Correction for Electrical Resistivity, *Tech. rep.*, USGS, 1–9.

Liu, X., and P. B. Flemings (2007), Dynamic multiphase flow model of hydrate formation in marine sediments, *Journal of Geophysical Research*, *112*(B3), B03,101, doi: 10.1029/2005JB004227.

MacGregor, L., and J. Tomlinson (2014), Special section : Interpretation and integration of CSEM data Marine controlled-source electromagnetic methods in the hydrocarbon industry : A tutorial on method and practice, *Interpretation*, *2*(3), 13–32.

Marín-Moreno, H., T. a. Minshull, G. K. Westbrook, B. Sinha, and S. Sarkar (2013), The response of methane hydrate beneath the seabed offshore Svalbard to ocean warming during the next three centuries, *Geophysical Research Letters*, *40*(19), 5159–5163, doi: 10.1002/grl.50985.

Marín-Moreno, H., T. Minshull, G. K. Westbrook, and B. Sinha (2015a), Estimates of future warming-induced methane emissions from hydrate offshore west Svalbard for a range of climate models, *Geochemistry, Geophysics, Geosystems*, *16*, 1307–1323, doi: 10.1002/2015GC005737.Received.

Marín-Moreno, H., M. Giustiniani, U. Tinivella, and E. Piñero (2015b), The Challenges of Quantifying the Carbon Stored in Arctic Marine Gas Hydrate, *Marine and Petroleum Geology*, *71*, 76–82, doi:10.1016j.marpetgeo.2015.11.014.

Mavko, G., M. T, and D. J (2009), *The Rock Physics Handbook*, 1–511 pp., Cambridge University Press, Cambridge, New York, Melbourne, Madrid, Cape Town, Singapore, Sao Paulo, Delhi, Dubai, Tokyo.

Minshull, T., M. Sinha, and C. Pierce (2005), Multi-disciplinary, sub-seabed geophysical imaging, *Sea Technology*, *46*(10), 27–31.

Montaron, B. (2009), Connectivity Theory -A New Approach To Modeling "Non-Archie" Rocks, *Petrophysics*, *50*(2), 102–115.

Murton, B., V. Huhnerbach, and J. Garrard (2012), Exploring Ultradeep Hydrothermal Vents In the Cayman Trough by ROV, *Sea Technology*, (September), 15–20.

735 Myer, D., S. Constable, and K. Key (2011), Broad-band waveforms and robust processing for marine CSEM surveys, *Geophysical Journal International*, *184*, 689–698, doi: 10.1111/j.1365-246X.2010.04887.x.

738 Myer, D., K. Key, and S. Constable (2015), Marine CSEM of the Scarborough Gas Field, *Geophysics*, *80*(3), E187–E196, doi:10.1190/1.3513870.

740 Panieri, G., C. A. Graves, and R. H. James (2016), Paleo-methane emissions recorded in foraminifera near the landward limit of the gas hydrate stability zone offshore western Svalbard, *Geochem. Geophys. Geosyst.*, *17*, 521–537, doi:10.1002/ 2015GC006153

743 Rajan, A., J. Mienert, and S. Bünz (2012), Acoustic evidence for a gas migration and release system in Arctic glaciated continental margins offshore NW-Svalbard, *Marine and Petroleum Geology*, *32*, 36–49, doi:10.1016/j.marpetgeo.2011.12.008.

746 Ramananjaona, C., L. MacGregor, and D. Andréis (2011), Sensitivity and inversion of marine electromagnetic data in a vertically anisotropic stratified earth, *Geophysical Prospecting*, *59*(2), 341–360, doi:10.1111/j.1365-2478.2010.00919.x.

749 Ray, A., and K. Key (2012), Bayesian inversion of marine CSEM data with a trans-dimensional self parametrizing algorithm, *Geophysical Journal International*, doi: 10.1111/j.1365-246X.2012.05677.x.

752 Reagan, M. T., and G. J. Moridis (2009), Large-scale simulation of methane hydrate dissociation along the West Spitsbergen Margin, *Geophysical Research Letters*, *36*(23), 1–5, doi:10.1029/2009GL041332.

755 Ritzmann, O., W. Jokat, W. Czuba, A. Guterch, R. Mjelde, and Y. Nishimura (2004), A deep seismic transect from Hovgard Ridge to northwestern Svalbard across the continental-ocean transition : A sheared margin study, *Geophysical Journal Interna-*

tional, *157*, 683–702, doi:10.1111/j.1365-246X.2004.02204.x.

Sahling, H., et al. (2014), Gas emissions at the continental margin west of Svalbard: mapping, sampling, and quantification, *Biogeosciences*, *11*(21), 6029–6046, doi:10.5194/bg-11-6029-2014.

Sarkar, S., C. Berndt, A. Chabert, D. G. Masson, T. A. Minshull, and G. K. Westbrook (2011), Switching of a paleo-ice stream in northwest Svalbard, *Quaternary Science Reviews*, *30*(13-14), 1710–1725, doi:10.1016/j.quascirev.2011.03.013.

Sarkar, S., C. Berndt, T. a. Minshull, G. K. Westbrook, D. Klaeschen, D. G. Masson, A. Chabert, and K. E. Thatcher (2012), Seismic evidence for shallow gas-escape features associated with a retreating gas hydrate zone offshore west Svalbard, *Journal of Geophysical Research*, *117*(B9), 1–18, doi:10.1029/2011JB009126.

Schmeling, H. (1986),Numerical models on the influence of partial melt on eleastic and anelastic and electrical properties of rocks. Part II: electrical conductivity, *Phys. Earth planet. Inter.*, *43*, 123–136.

Schwalenberg, K., E. Willoughby, R. Mir, and R. N. Edwards (2005), Marine gas hydrate electromagnetic signatures in Cascadia and their correlation with seismic blank zones, *First Break*, *23*(April), 57–63.

Schwalenberg, K., M. Haeckel, J. Poort, and M. Jegen (2010a), Evaluation of gas hydrate deposits in an active seep area using marine controlled source electromagnetics : Results from Opouawe Bank , Hikurangi Margin , New Zealand, *Marine Geology*, *272*(1-4), 79–88, doi:10.1016/j.margeo.2009.07.006.

Schwalenberg, K., W. Wood, I. Pecher, L. Hamdan, S. Henrys, M. Jegen, and R. Coffin (2010b), Preliminary interpretation of electromagnetic, heat flow, seismic, and geochemical data for gas hydrate distribution across the Porangahau Ridge, New Zealand, *Marine Geology*, *272*(1-4), 89–98, doi:10.1016/j.margeo.2009.10.024.

Sinha, M. C., P. D. Patel, M. J. Unsworth, T. R. E. Owen, M. R. G. Maccormack, and M. Road (1990), An Active Source Electromagnetic Sounding System for Marine Use, *Marine Geophysical Researches*, *12*, 59–68.

Smith, B. D., and S. H. Ward (1974), On the Computation of Polarization Ellipse Parameters, *Geophysics*, *39*(6), 867–869.

Solheim, A., E. Andersen, A. Elverhoi, and A. Fiedler (1996), Late Cenozoic depositional history of the western Svalbard continental shelf, controlled by subsidence and climate, *Global and Planetary Change*, *12*, 135–148.

Thatcher, K. E., G. K. Westbrook, S. Sarkar, and T. A. Minshull (2013), Methane release from warming-induced hydrate dissociation in the West Svalbard continental margin : Timing, rates, and geological controls, *Journal of Geophysical Research*, *118*, 1–17, doi:10.1029/2012JB009605.

Vogt, P. R., K. Crane, E. Sundvor, M. D. Max, and S. L. Pfirman (1994), Methane-generated (?) pockmarks on young, thickly sedimented oceanic crust in the Arctic: Vestnesa ridge, Fram strait, *Geology*, *22*, 255–258, doi:10.1130/0091-7613(1994)022<0255.

Waxman, M. H. and Smits, L. J. M. (1968), Electrical conductivities in oil-bearing shaly sands, *Soc. Pet. Eng. J.*, *8*, 107–122.

Weitemeyer, K., and S. Constable (2010), Mapping shallow geology and gas hydrate with marine CSEM surveys, *First Break*, *28*(June), 97–102.

Weitemeyer, K., S. Constable, and K. Key (2006a), Marine EM techniques for gas-hydrate detection and hazard mitigation, *The Leading Edge*, (May), 629–632.

Weitemeyer, K. A., S. C. Constable, K. W. Key, and J. P. Behrens (2006b), First results from a marine controlled-source electromagnetic survey to detect gas hydrates offshore Oregon, *Geophysical Research Letters*, *33*(L03304), 1–4, doi:10.1029/2005GL024896.

Weitemeyer, K. A., S. Constable, and A. M. Tréhu (2011), A marine electromagnetic survey to detect gas hydrate at Hydrate Ridge, Oregon, *Geophysical Journal International*, *187*(1), 45–62, doi:10.1111/j.1365-246X.2011.05105.x.

Westbrook, G., et al. (2008), Estimation of gas hydrate concentration from multi-component seismic data at sites on the continental margins of NW Svalbard and the Storegga region of Norway, *Marine and Petroleum Geology*, *25*(8), 744–758, doi: 10.1016/j.marpetgeo.2008.02.003.

Westbrook, G. K., et al. (2009), Escape of methane gas from the seabed along the West Spitsbergen continental margin, *Geophysical Research Letters*, *36*(15), 1–5, doi: 10.1029/2009GL039191.

Line Name	Inversion type	Receiver type	Data type	Target misfit	Iterations
Line 1	Isotropic	OBE	Log Amplitude, phase	1	13
Line 1	VTI	OBE	Log Amplitude, phase	0.88	9
Line 1	Isotropic	Vulcan	P_{max}	1	13
Line 1	VTI	Vulcan	P_{max}	1	11
Line 2	Isotropic	Vulcan	P_{max}	1	10
Line 2	VTI	Vulcan	P_{max}	1	9

Table 1. Detail of OBE and Vulcan inversions for the resistivity models shown for Line 1 and Line 2.

Thickness (m)	True (Ωm^2)	Recovered (Ωm^2)	Conductor depth (m)
100	300	317	150
150	450	410	180
200	600	520	250
250	750	542	310
300	900	751	$<0.4\ \Omega$m not recovered
350	1050	1010	$<0.4\ \Omega$m not recovered

Table 2. Transverse resistance calculations for the synthetic model and inverted models shown in Figure 8a. The transverse resistances are estimated using a resistivity of 3 Ωm and thickness interval beneath the seafloor shown in column 1.

Thickness (m)	True (Ωm^2)	Recovered (Ωm^2)	Resistor depth (m)
100	100	112	240
150	150	151	250
200	200	217	250
250	250	305	300
300	300	298	$>3.3\ \Omega$m not recovered
350	350	343	$>3.3\ \Omega$m not recovered

Table 3. Transverse resistance calculations for the synthetic model and inverted models shown in Figure 8b. The transverse resistances are estimated using a resistivity of 1 Ωm and thickness interval beneath the seafloor shown in column 1.

Line Name	Depth interval	Model Distance	Porosity	Archie (%)	Lee (%)	Constituent
Line 1	seabed–BSR	0–2 km	∼45%	25–60	20–55	Hydrate
Line 1	seabed–BSR	3.5–8 km	45–47%	20–40	15–35	Hydrate
Line 1	seabed–BSR	8–10.5 km	47–49%	20–50	15–45	Hydrate
Line 1	seabed–BSR	8–10.5 km	35%	2–22	0–12	Hydrate
Line 1	seabed+ 200 m	10.5–13.5 km	∼45%	20–55	15–50	Free gas
Line 1	seabed+ 200 m	10.5–13.5 km	35%	5–40	2–30	Free gas
Line 2	seabed+ 200 m	0–1 km	∼45%	25–55	20–50	Free gas
Line 2	seabed+ 200 m	0–1 km	35%	10–35	8–30	Free gas
Line 2	seabed–BSR	1–3 km	46–47%	10–35	4–25	Hydrate
Line 2	seabed–BSR	1–3 km	35%	0–10	0–8	Hydrate

Table 4. Shallow Hydrate and free gas saturations inferred for Line 1 and Line 2 using two different methods, Archie's Law [*Archie*, 1942] (column 5) and a connectivity equation [*Lee*, 2011] (column 6).

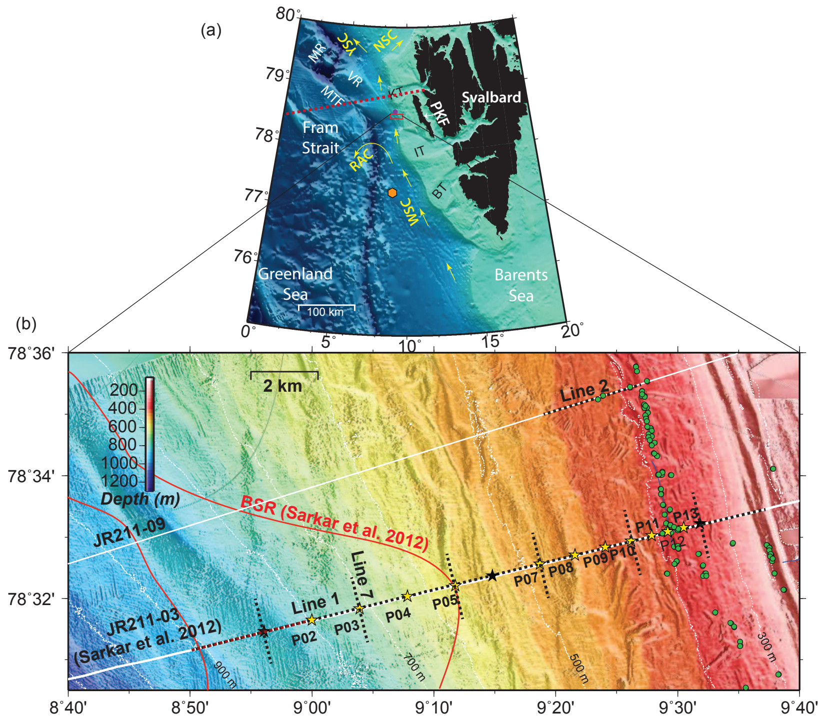

Figure 1. (a) Map of west Svalbard showing the continental slope survey area on the regional bathymetry map from international bathymetric chart of the Arctic Ocean (IBCAO) data [*Jakobsson et al.*, 2008]. The regional velocity models obtained from seismic refraction data shown by the dotted red line -AWI-994000 [*Ritzmann et al.*, 2004] are used to infer basement depth for the study area. MR- Molloy Ridge, MTF- Molloy Transform Fault, VR-Vestnesa Ridge, PKF-Prins Karl Forland. Ocean currents: WSC - West Spitsbergen Current, NSC - North Spitsbergen Current, YSC - Yermak Slope Current and RAC - Return Atlantic Current and cross-shelf troughs: KT- Kongsfjorden Trough, IS - Isfjorden Tough, BT - Bellsund Trough effect the sedimentaion. ODP Site 986 (orange polygon) provides reference resistivity and porosity. (b) Location of coincident CSEM (dotted black line) and seismic reflection survey lines (white lines) with multibeam bathymetry data. Green dots are the positions of the methane seeps observed in 2008. Ocean bottom electric-field (OBE) (yellow stars) record the CSEM data and the black stars show the OBEs that were not used for the CSEM inversion due to instrument errors. Initial 4.2 km (red dashed line) of Line 1 was discarded due to unknown DASI tow height.

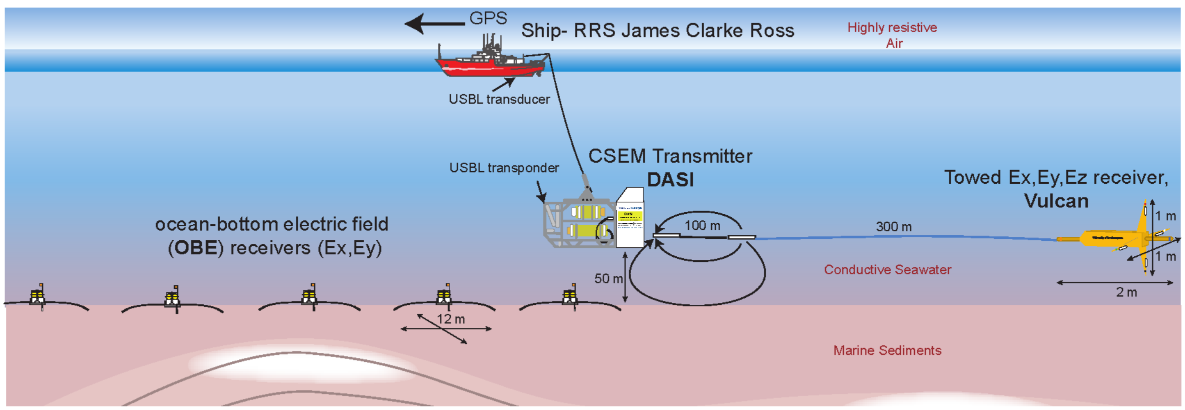

Figure 2. Sketch of the CSEM instrument layout used in the 2012 survey. CSEM transmitter, DASI was towed 50m above the seafloor and transmitted a 81A current across its 100m dipole. Towed receiver, Vulcan was attached 300m behind the DASI antenna and recorded the transmitted EM signal along with the seafloor EM receivers, OBEs (reproduced from *Goswami et al.* [2015]).

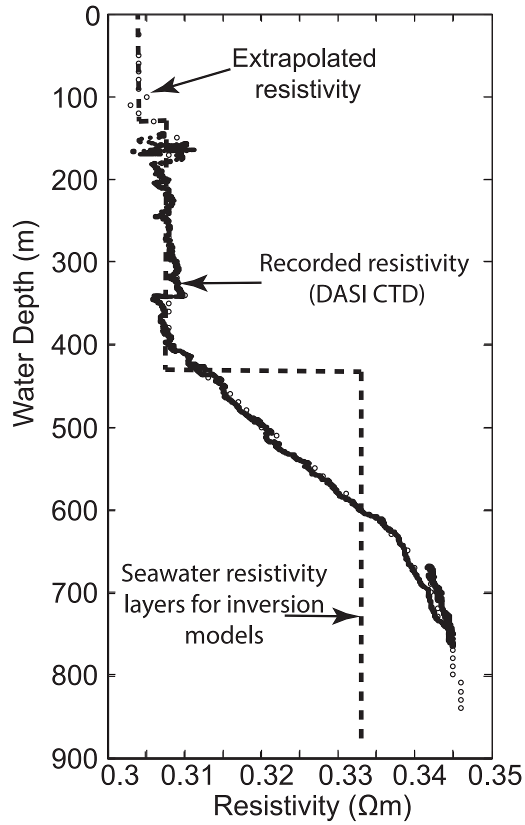

Figure 3. Resistivity of the water column obtained from the CTD mounted on DASI frame during its operation on Line 1. There is no information from the CTD above 150 m as the CTD was switched off at 150 m beneath the sea-surface.

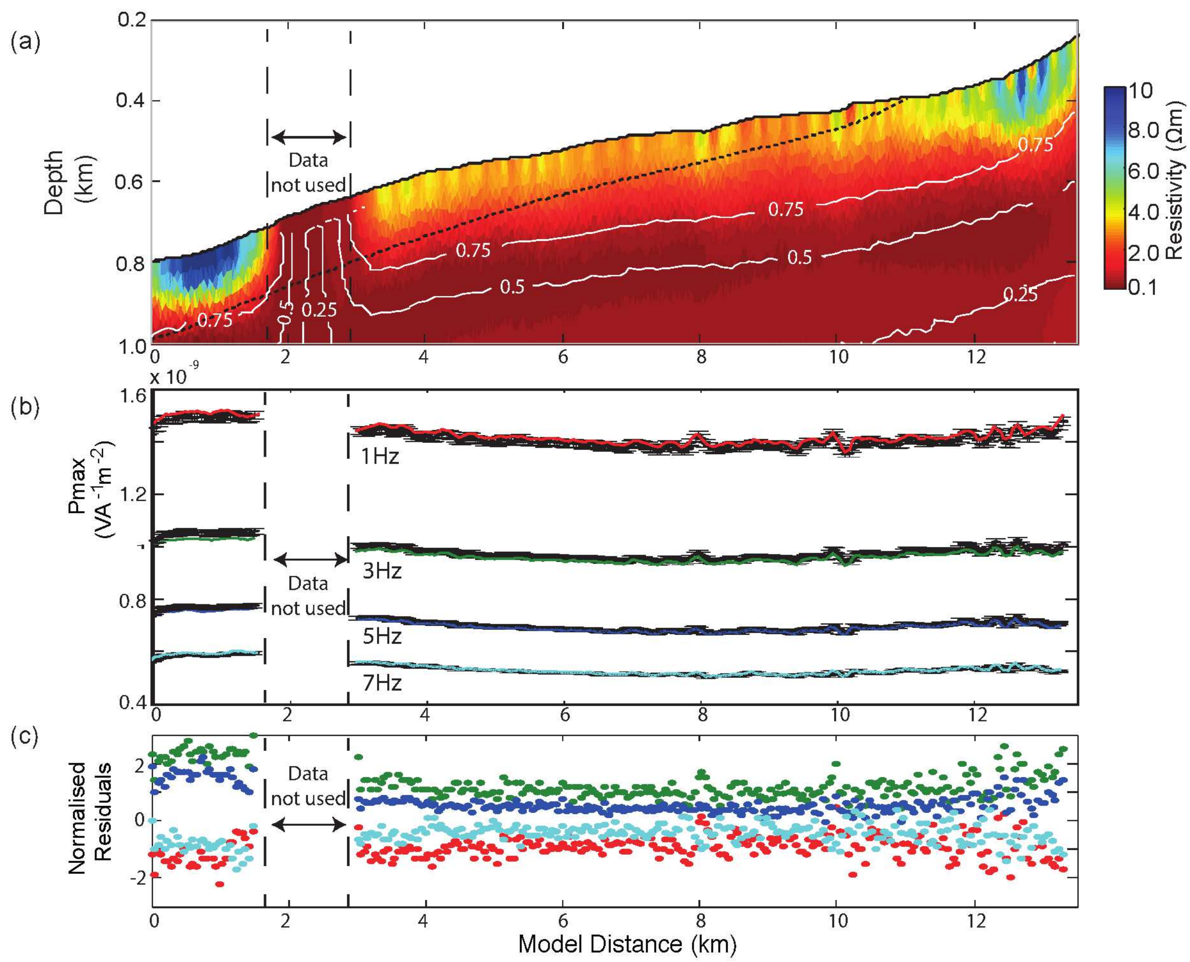

Figure 4. (a) Vertical resistivity model obtained from VTI inversion of Vulcan P_{max} data for Line 1 showing significant lateral variation in resistivity. The predicted base of GHSZ from *Marín-Moreno et al.* [2013] is shown as a dashed line. Noisy data between 1.8–3 km model distance were not included in the inversion. Contour overlay (thin white line) shows data sensitivity to model features (0.5=50% sensitivity). (b) Data (dots) and model (solid lines: 1 Hz–red, 3 Hz–green, 5 Hz–blue, 7 Hz–cyan) shows a good fit of the anisotropic model. (c) The residuals (1 Hz–red, 3 Hz–green, 5 Hz–blue, 7 Hz–cyan) normalised by their respective data error are collectively scattered around 0. However, a slight bias can be observed at each individual frequency likely related to the unknown dip of DASI antenna.

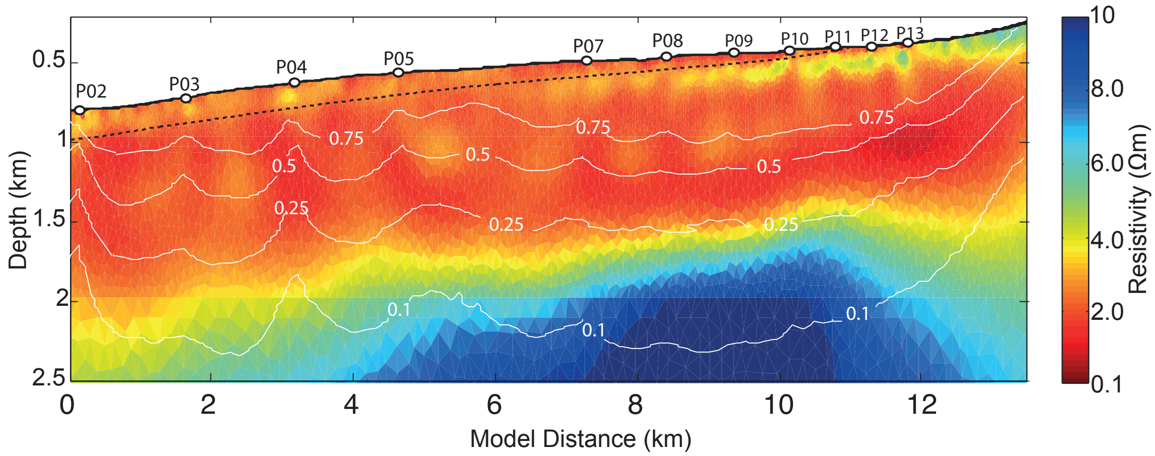

Figure 5. Vertical resistivity model for Line 1 obtained from VTI inversion of OBE amplitude and phase data. The predicted base of GHSZ from *Marín-Moreno et al.* [2013] is shown as a dashed line. Contour overlay (thin white line) shows data sensitivity to model features (0.5=50% sensitivity).

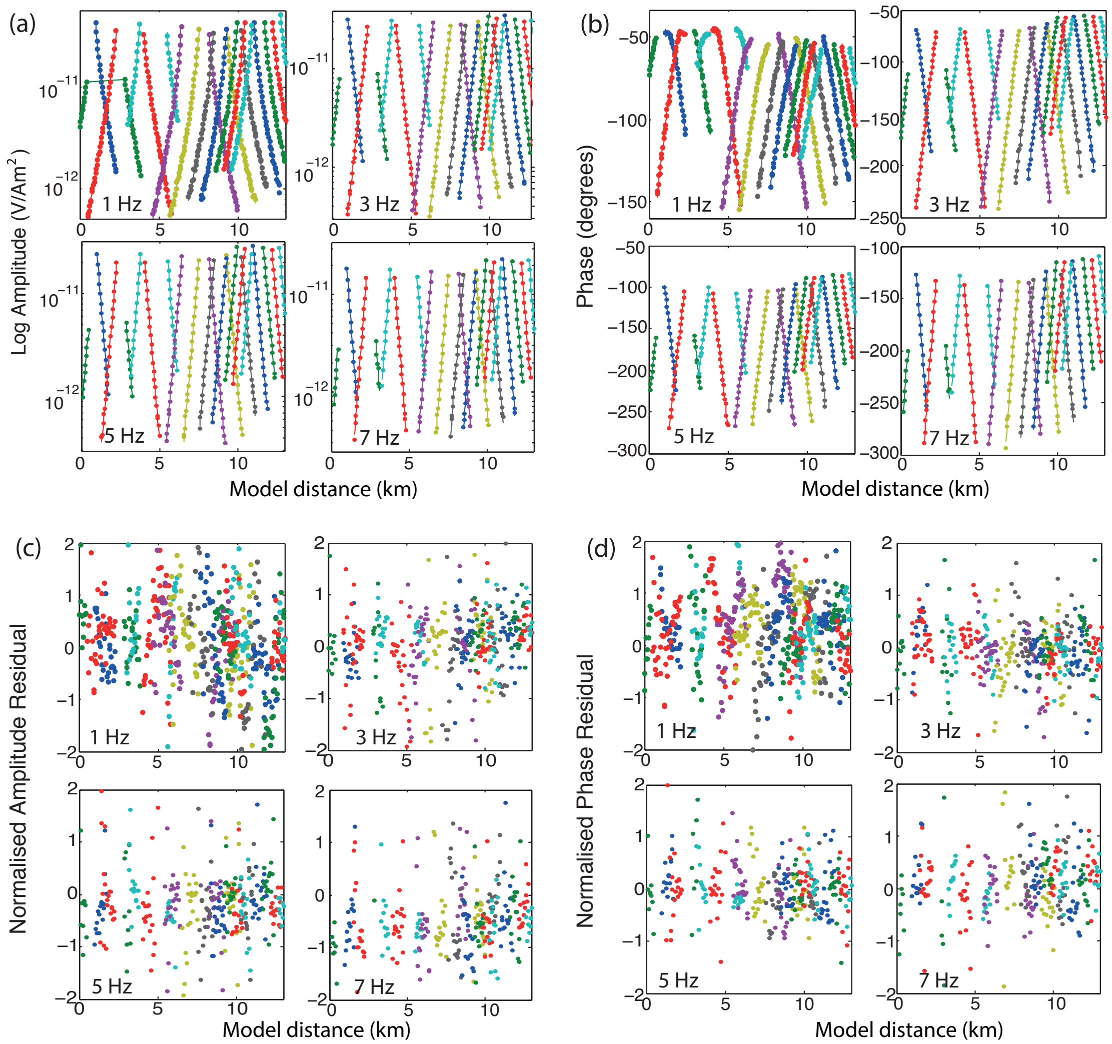

Figure 6. This figure shows the model (solid lines) fit to OBE data (solid circles) for 1, 3, 5, 7 Hz frequencies used in the inversion. (a) Amplitude (error bars are too small in the log scale display to be visible), (b) phase, (c) normalised amplitude residuals and (d) normalised phase residuals show a good model to data fit for the target misfit of 0.88 and 3% data uncertainty. The residuals are normalised by their respective data error. A gradual increase in amplitude and phase towards the end of the line is also observed in the data as seen by the higher resistivity in the resistivity models shown in Figure 5.

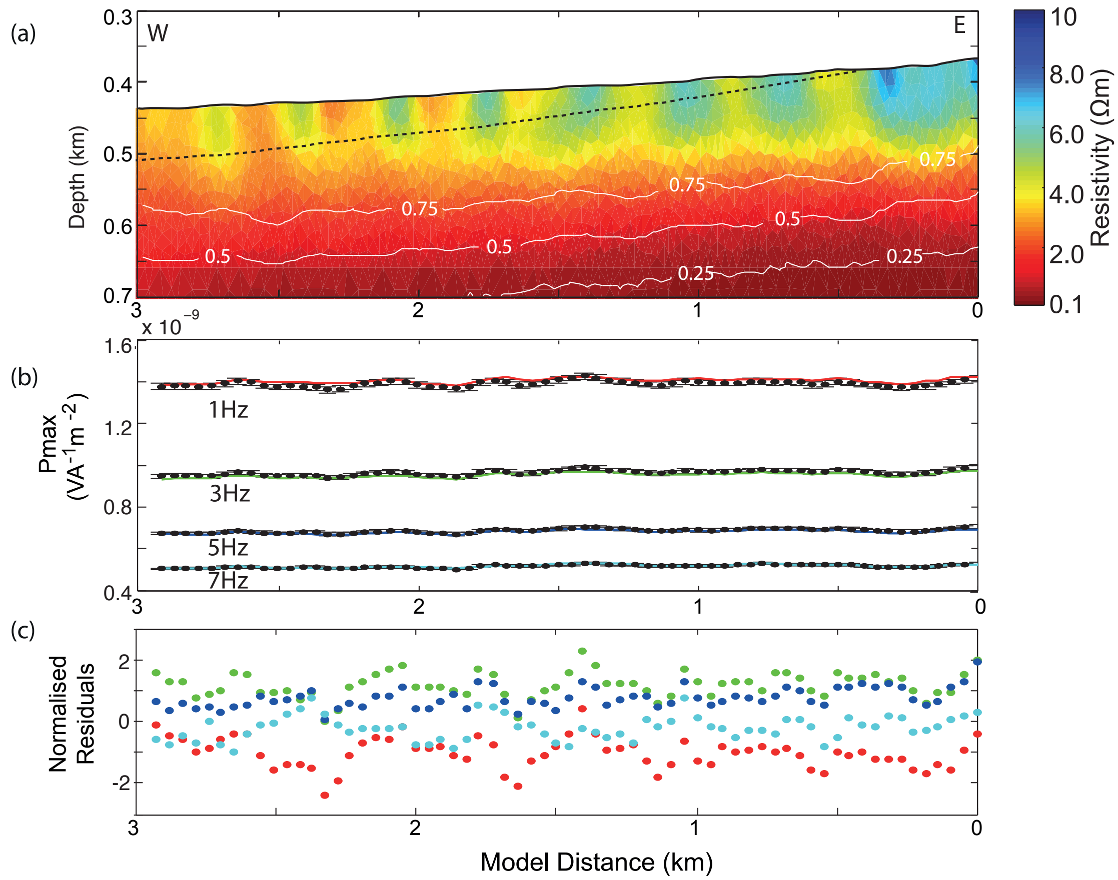

Figure 7. (a) Vertical resistivity model obtained from VTI inversion of Vulcan P_{max} data for Line 2. The predicted base of GHSZ obtained using estimates of *Marín-Moreno et al.* [2013] is shown as a dashed line. Contour overlay (thin white line) shows data sensitivity to model features (0.5=50% sensitivity). (b) Data (dots) with error bars and model fit (solid lines: 1 Hz–red, 3 Hz–green, 5 Hz–blue, 7 Hz–cyan). (c) The residuals (1 Hz–red, 3 Hz–green, 5 Hz–blue, 7 Hz–cyan) normalised by their respective data error are collectively scattered around 0. However, a slight bias can be observed at each individual frequency likely related to the unknown dip of the DASI antenna.

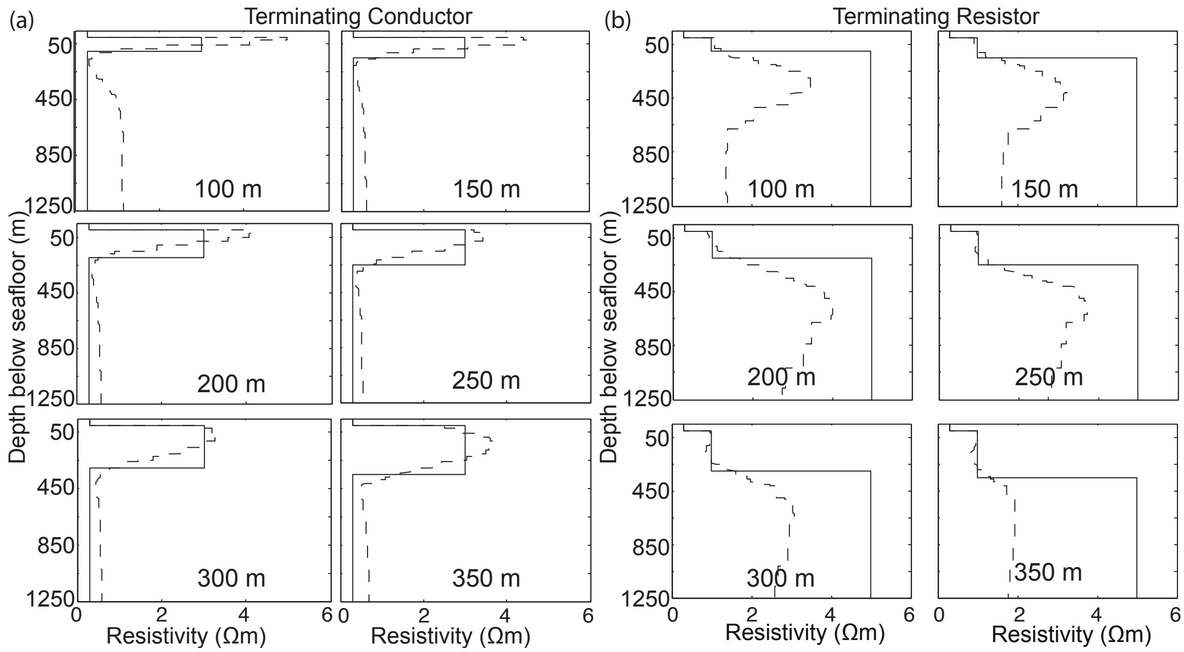

Figure 8. (a) Synthetic models showing different depths to the terminating 0.3 Ωm conductor beneath a 3 Ωm resistor. (b) Synthetic models showing different depths to the terminating 5 Ωm resistor beneath a 1 Ωm resistor. The true models are shown by the solid lines and the 2D inversion results are shown by the dashed lines. The test suggests 250 m depth sensitivity for Vulcan.

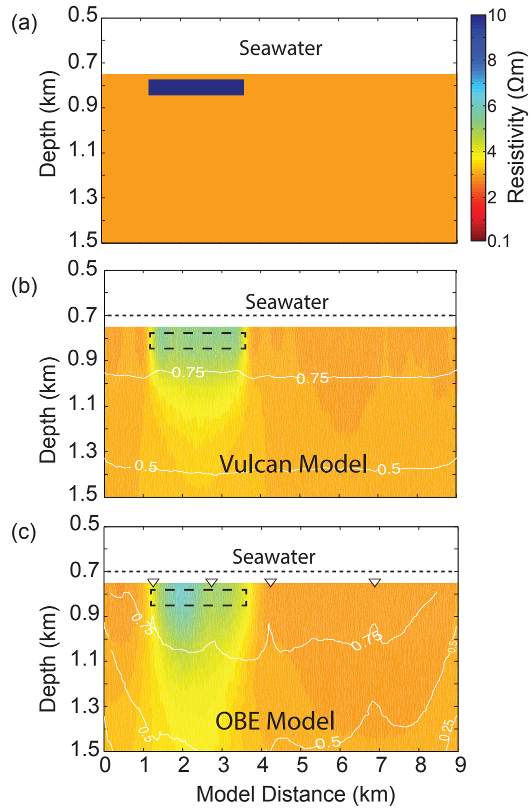

Figure 9. Synthetic models showing sensitivity of OBE and Vulcan data to shallow resistors. (a) The synthetic model contains a 2.2 km long, 100 m thick 10 Ωm resistor buried 50 m beneath the seafloor. (b) P_{max} inversion of synthetic Vulcan data. DASI and Vulcan are shown by the dashed line. (c) Amplitude and phase inversion of synthetic OBE data for OBE locations shown by triangles and DASI height shown by the dashed line. Sensitivity of data to model are shown by the sensitivity contours (white lines: e.g. 0.5=50% sensitivity) in panels (b) and (c). Data between 0 and 850 m transmitter-receiver offset for OBE data were not used in these synthetic inversions in order to simulate the real data available for inversion. The Vulcan model recovers the buried resistor slightly better than the OBE model. However, both OBE and Vulcan models underestimate the resistivity of the 10 Ωm resistor.

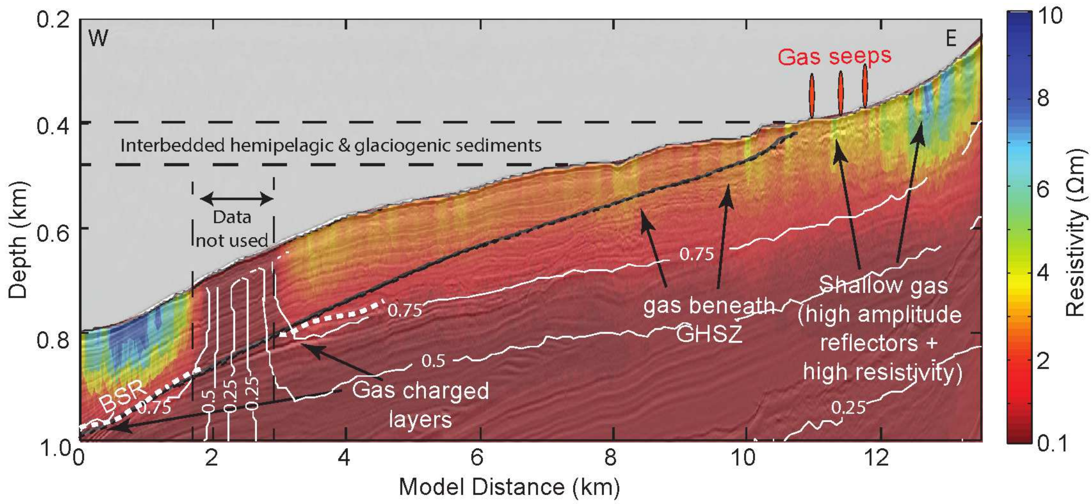

Figure 10. Overlay of vertical resistivity model from Vulcan inversion on coincident seismic reflection data for Line 1 (JR211-03 [*Sarkar et al.*, 2012]) showing high resistivities above the BSR and bright amplitude reflectors associated with free gas. The dashed line marks the base of the GHSZ as per models of *Marín-Moreno et al.* [2013]. Contour overlay (thin white line) shows data sensitivity to resistivity model (0.5=50% sensitivity)

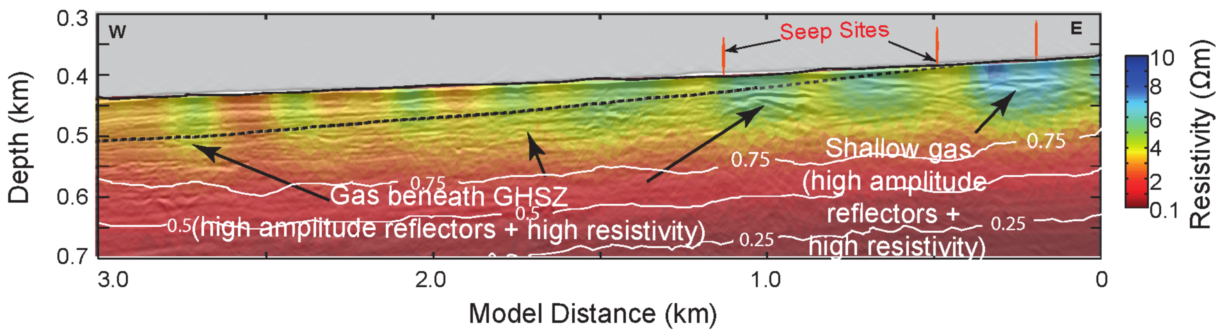

Figure 11. Overlay of vertical resistivity model from Vulcan inversion on coincident seismic reflection data for Line 2 (JR211-09 [*Sarkar et al.*, 2012]) shows high resistivites within the shallow sediments. High amplitude reflectors associated with free gas are also observed on the seismic reflection data. The dashed line marks the base of the GHSZ from *Marín-Moreno et al.* [2013]. Contour overlay (thin white line) shows data sensitivity to resistivity model (0.5=50% sensitivity)

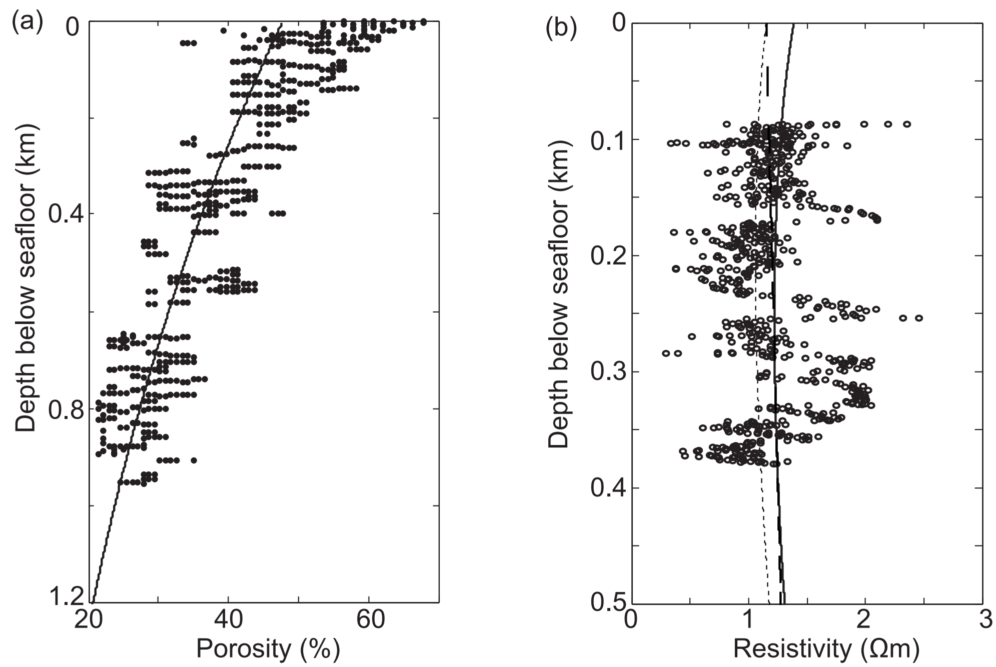

Figure 12. (a) A least squares exponential fit (solid line) to the ODP porosity log (solid dots) [*Jansen et al.*, 1996] is used for estimating saturation estimates for our study area. (b) Least squares linear fit (dashed line) to the ODP resistivity log (circles) [*Jansen et al.*, 1996] provide the background resistivity trend for water saturated sediments for our study area. Reasonable fits to this background trend can be obtained using Archie's equation (dotted line) for coefficients m=n=2 and a=1 and for the connectivity equation (solid line) of *Lee* [2011] using α=3 and μ=2.

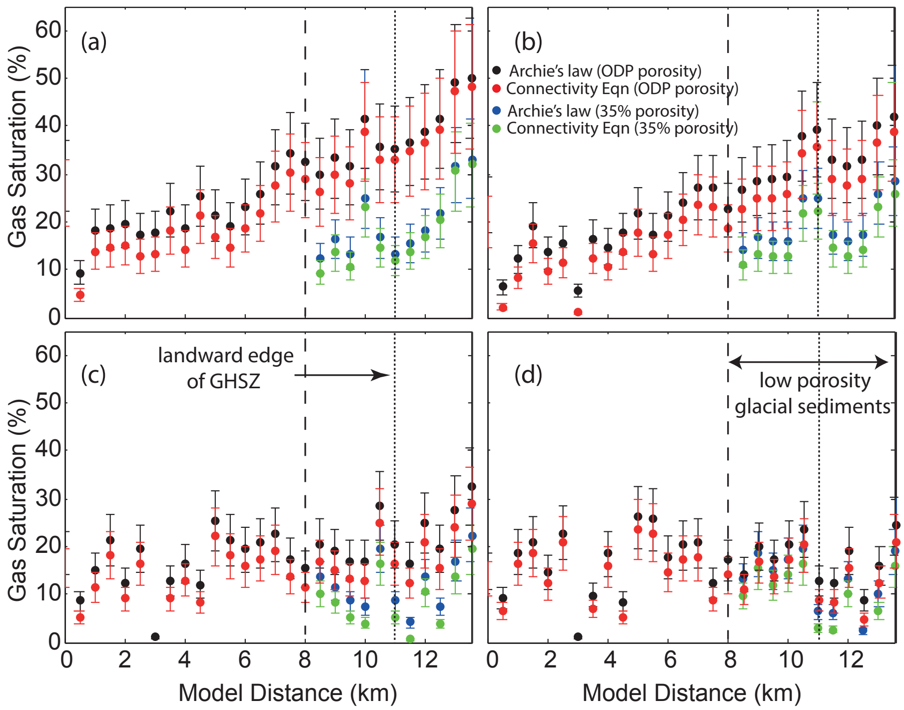

Figure 13. Depth averaged free gas saturation for incremental 100 m thick layers beneath the predicted base of gas hydrate stability zone. (a) 0–100 m beneath the GHSZ, (b) 100–200 m beneath GHSZ, (c) 200–300 m beneath GHSZ and (d) 300–400 m beneath the GHSZ. Between 10.5 (dotted vertical line) and 13.5 km model distance, the thickness of the GHSZ is 0 m. Depth averaged porosities from ODP Site 986 (Figure 12a) are used to obtain saturation estimates for each depth interval (Black dots – Archie's law; Red dots – Connectivity equation [*Lee*, 2011]). Between 8 –13.5 km model distance, a constant 35% porosity is assumed for alternative saturation estimates to account for low porosity glacial sediments (Blue dots – Archie's law; Green dots – Connectivity equation). Vertical dashed line at 8 km model distance marks the seaward extent of the lower porosity (35%) glacial sediments.

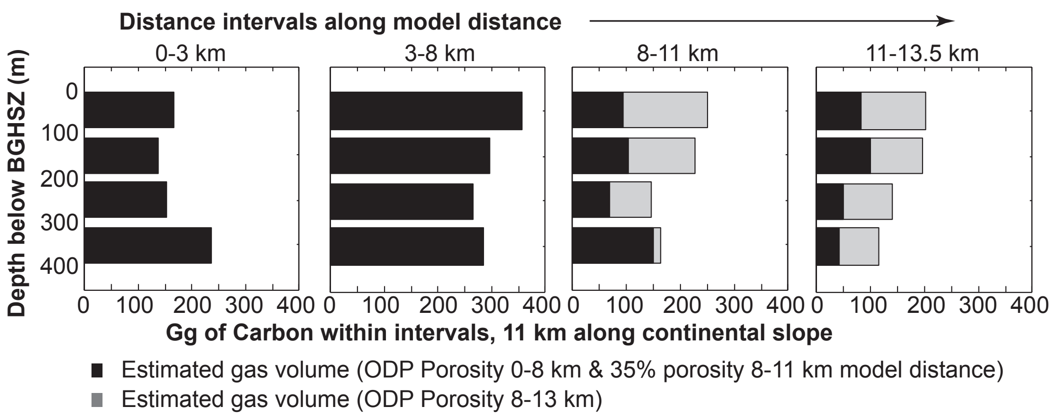

Figure 14. Estimated amounts of carbon present as methane within 100 m depth intervals beneath the base of GHSZ (as shown in Figure 13) using average saturation values (from connectivity equation) derived from Figure 13 for a 11 km long strip along the continental slope.

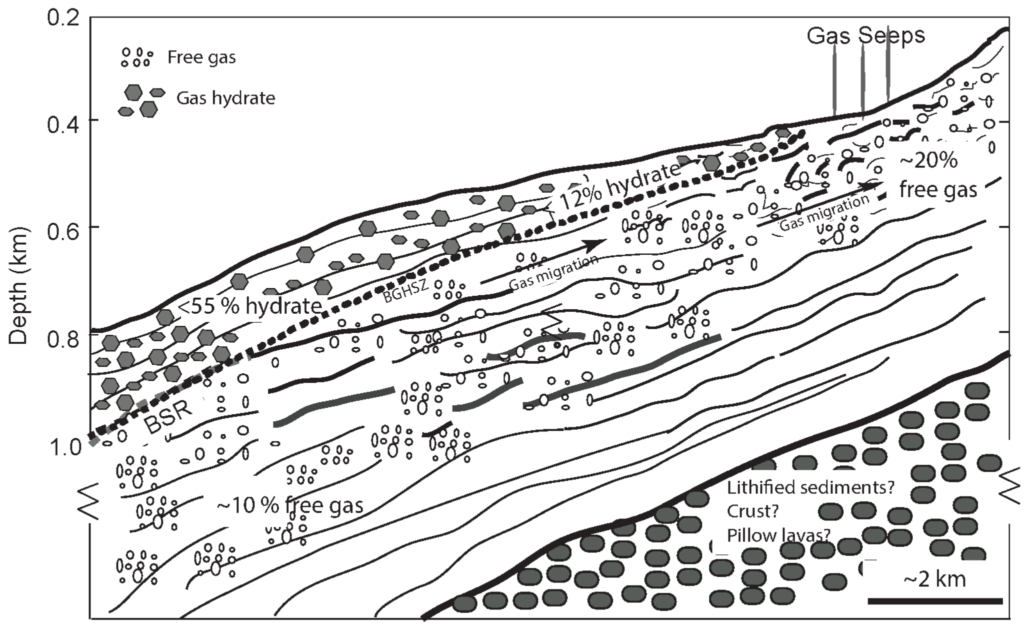

Figure 15. A sketch of the study area showing interpretations of hydrate and gas in the continental slope offshore Svalbard based on CSEM and seismic data. The vertical axis in the lower part of the figure is not to scale. Up to 12% hydrate near the landward edge of the GHSZ and 15–55% hydrate in the lower slope are inferred. Wide spread presence of free gas beneath the GHSZ is also inferred in the area.

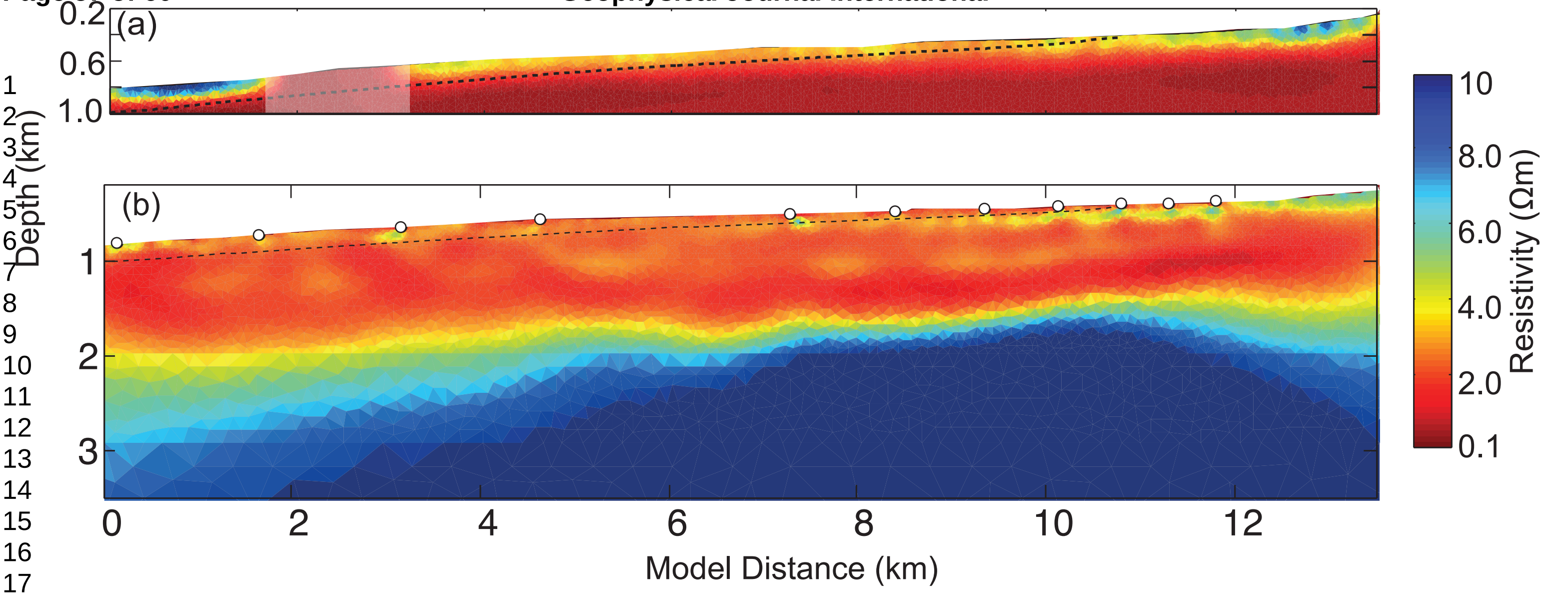

Figure S.1: Isotropic resistivity models for Line 1 obtained from inversion of (a) Vulcan P-max data and (b) amplitude and phase OBE data shows high level of similarity to vertical resistivity models obtained from TIZ anisotropic inversion.

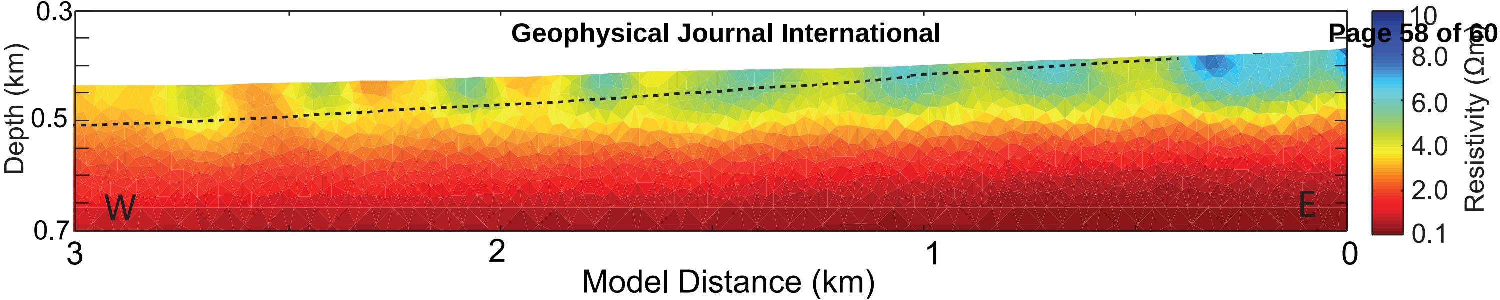

Figure S.2: Isotropic resistivity model for Line 2 obtained from inversion of Vulcan P-max data shows high level of similarity to vertical resistivity models obtained from TIZ anisotropic inversion.

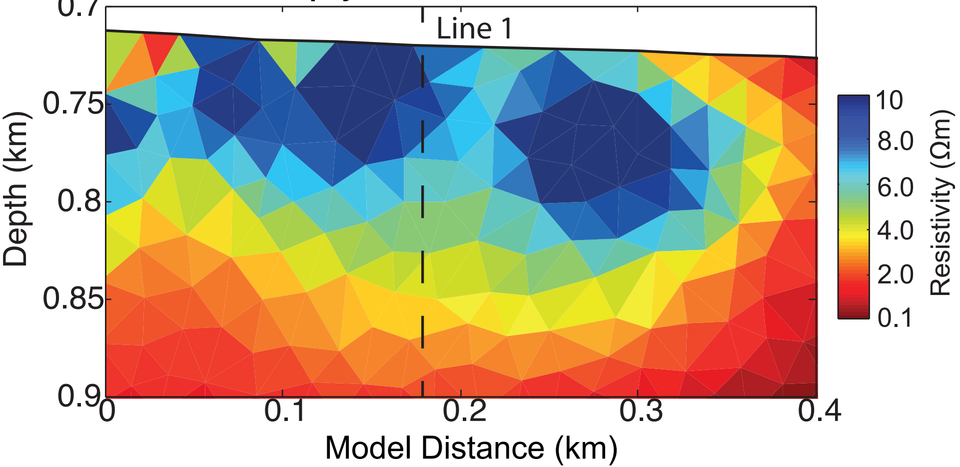

Figure S.3: Vertical resistivity model (VTI anisotropic) for Line 7, shows high resistivities similar to that observed between 0-2 km model distance on Line 1.

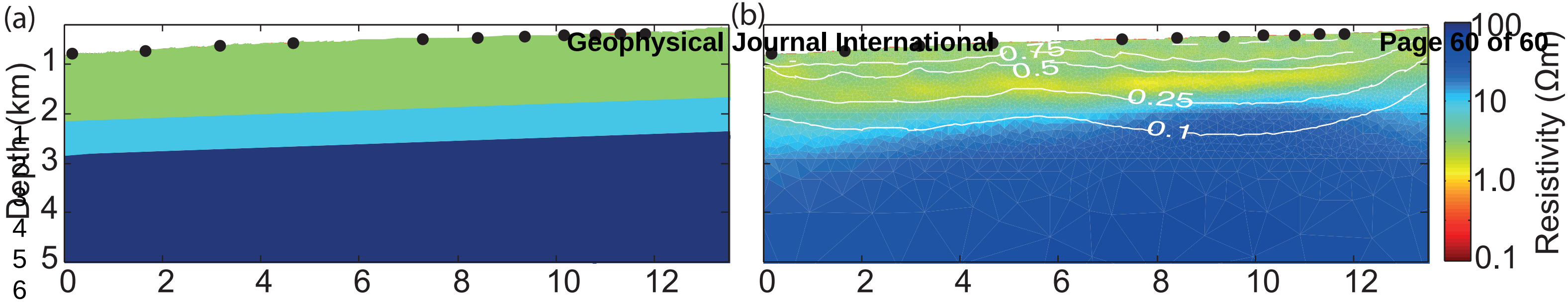

Figure S.4: (a) Synthetic model containing a 500 m thick 10 Ωm resistor 1.5 km beneath the seabed. This is followed by a 100 Ωm halfspace. (b) Inversion of synthetic data was able recover the 10 Ωm resistor in presence of the high resisitivity half space beneath.